

# **Analysis of X-radiation in the module calibration setup and Vcal calibration with filters**

Maren Tabea Meinhard  
Institute for Particle Physics - ETH Zürich

August 29, 2014

*Supervisors:* Prof. Dr. Rainer Wallny  
Institute for Particle Physics - ETH Zürich  
Dr. Andrey Starodumov  
Institute for Particle Physics - ETH Zürich  
Jan Hoß  
Institute for Particle Physics - ETH Zürich

## Abstract

The CMS pixel detector is made of components called modules. Each module consists of several components including a silicon sensor that detects charged particles to determine their track and momentum. These modules need to be energy calibrated before being installed in the detector to know the amount of charge deposited in the detector that corresponds to the output signal. For this so-called Vcal calibration, modules are irradiated with monochromatic X-radiation which is emitted by secondary emission from target materials. The precisely known energy of the emission lines of this X-radiation is taken as a reference energy for the calibration. The aim of this work is to study if the setup which is used for the Vcal calibration can be optimized. It is studied if the X-radiation is isotropic and if it is modified by filters. Then, a Vcal calibration of modules is carried out with and without filters to determine if filters have an impact on the Vcal calibration. Moreover, the best possible emplacement of the test setup for modules is found in order to have a homogeneous hit rate on the four available test positions.

It has been found that while the intensity of the X-radiation decreases with increasing distance to the target materials, the energy of the emission lines is independent of it. It has also been verified that the  $K_\beta$  emission line from target materials can be removed using filters. On spectra measured with a single chip module, the  $K_\alpha$  and  $K_\beta$  peaks are combined to a single energy peak due to the coarse energy resolution of the chip. Therefore, the removal of the  $K_\beta$  line with filters is expected to reduce the width of the energy peak in the spectrum and to shift the mean of the peak to lower energies than without filters. This has been verified for the Molybdenum (Mo) target but not for the Tin (Sn) target where the mean of the peak is at higher energies than without filter. Consequently, for a single chip module, the slope of the Vcal calibration is slightly reduced and the offset is increased when filters are used. For the digital module which has been tested the addition of filters did not have a significant impact on the Vcal calibration. Based on the results for the digital module which has 16 times more statistics than the single chip module, it does not seem necessary to include filters in the setup. After moving the test setup for modules, the hit rate on the module coming from the primary X-ray beam is homogeneous over the two middle but decreases on the two outer ones. By increasing the tube voltage for measurements on the two exterior positions, the same hit rate can be achieved on all positions. The hit rate coming from the fluorescence of the target materials is slightly decreasing for positions further away from the source of the secondary emission.

# Contents

<b>1</b>	<b>Introduction - LHC and CMS</b>	<b>7</b>
<b>2</b>	<b>CMS pixel detector</b>	<b>9</b>
2.1	The CMS readout chip (ROC) . . . . .	10
2.2	Pixel detector modules . . . . .	11
2.3	Energy calibration . . . . .	12
<b>3</b>	<b>Measurements of the X-radiation with spectrometer</b>	<b>16</b>
3.1	X-ray setup for module calibration . . . . .	16
3.2	Spectrometer X-123 from Amptek . . . . .	17
3.3	X-ray spectra measured with spectrometer . . . . .	17
3.3.1	Isotropy of the X-ray illumination . . . . .	19
3.3.2	Background reduction with filters . . . . .	22
3.3.2.1	Spectrum in the centre . . . . .	22
3.3.2.2	Influence of filters on the spectra . . . . .	26
<b>4</b>	<b>Impact of filters on Vcal calibration</b>	<b>31</b>
4.1	Effect of filters on spectra measured with a single chip module . . . . .	31
4.2	Effect of filters on the Vcal calibration of a digital readout chip . . . . .	35
4.3	Vcal calibration of a digital module with and without filters . . . . .	35
<b>5</b>	<b>Homogeneity of the X-ray illumination on the module test positions</b>	<b>40</b>
<b>6</b>	<b>Conclusions and outlooks</b>	<b>46</b>
6.1	Key results . . . . .	46
6.2	Further work and outlooks . . . . .	47
	<b>Appendix</b>	<b>49</b>

# List of Figures

1	CMS . . . . .	8
2	Silicon pixel detector . . . . .	10
3	ROC structure . . . . .	11
4	ROC readout chain . . . . .	13
5	ROC readout . . . . .	14
6	Modules for pixel detector upgrade . . . . .	14
7	Digital module . . . . .	14
8	PH calibration . . . . .	15
9	Picture source and targets . . . . .	17
10	Picture filter holder . . . . .	18
11	Positions for analysis in X-ray box . . . . .	18
12	Spectra LF and LB . . . . .	20
13	Spectra RF and RB . . . . .	21
14	Spectra without aluminium at the centre . . . . .	24
15	Spectrum with aluminium at the centre . . . . .	24
16	Spectrum with filter Mo . . . . .	27
17	Spectrum with filter Ag . . . . .	27
18	Spectrum with filter Sn . . . . .	28
19	Spectrum with filter Cu . . . . .	28
20	Spectra from single chip module Mo . . . . .	32
21	Spectra from single chip module Ag . . . . .	32
22	Spectra from single chip module Sn . . . . .	32
23	Fits for spectra from single chip module . . . . .	33
24	$\sigma$ for the fits with and without filter of Mo, Ag, Sn . . . . .	34
25	Mean for the fits with and without filter of Mo, Ag, Sn . . . . .	34
26	Vcal calibration ROC . . . . .	36
27	Numbering of ROCs . . . . .	37
28	Slope values Vcal module without filter . . . . .	38
29	Slope values Vcal module with filter . . . . .	38
30	Offset values Vcal module without filter . . . . .	38

31	Offset values Vcal module with filter . . . . .	38
32	$\chi^2$ values Vcal module without filter . . . . .	39
33	$\chi^2$ values Vcal module with filter . . . . .	39
34	Comparison spectra ROC / Spectrometer . . . . .	39
35	Hit map primary beam . . . . .	41
36	Hit map primary beam with masked rows . . . . .	41
37	Test positions for module . . . . .	41
38	Hit rates primary beam - old emplacement . . . . .	44
39	Hit rates primary beam - new emplacement . . . . .	44
40	Hit rates Mo . . . . .	45
41	Hit rates Sn . . . . .	45

## List of Tables

1	Peak integral LF, LB, RF, RB . . . . .	22
2	Peak energy for $K_{\alpha}$ line for all positions . . . . .	23
3	Peak integral with/without aluminium foil . . . . .	25
4	Peak energy for $K_{\alpha}$ line with and without aluminium foil on the spectrometer . . . . .	25
5	Filter choice . . . . .	29
6	Effect of filters on spectra . . . . .	29
7	Hit rates on the module . . . . .	44

# 1 Introduction - LHC and CMS

One of the world's largest centres for research in physics is CERN (Organisation Européenne pour la Recherche Nucléaire) located in Geneva, Switzerland. Most of its experiments are designed to study particle physics, however, others also involve nuclear, medical or atmospheric physics. CERN has operated several particle accelerators, including the LEP (Large Electron-Positron collider) which was dismantled in 2001, the SPS (Super Proton Synchrotron) and most well-known the LHC (Large Hadron Collider), both of which are in use nowadays.

The LHC, which became operational in 2009 has a circumference of around 27 km and accelerates two proton beams to create collisions between quarks and gluons. It has a design centre of mass energy of 14 TeV. Four experiments are distributed around the LHC ring. ALICE is looking for a quark-gluon plasma that might have existed shortly after the Big Bang and LHCb is looking for explanations for the matter-antimatter asymmetry in the universe. CMS (Compact Muon Solenoid) and ATLAS are multiple purpose detectors. They have discovered a Higgs boson in 2012 [1,2] and are involved in the search for extra dimensions and particles that could explain dark matter.

The innermost component of CMS is a tracker detector which detects charged particles. It consists of a pixel and of a microstrip silicon detector. Further away from the beam line there is an electromagnetic and a hadronic calorimeter. A solenoid magnet which produces a 4 T magnetic field to bend charged particle's tracks encloses them all [4]. Finally, muons that were produced in the collisions are tracked by muon chambers outside of the solenoid (Figure 3).

## CMS DETECTOR

Total weight : 14,000 tonnes  
Overall diameter : 15.0 m  
Overall length : 28.7 m  
Magnetic field : 3.8 T

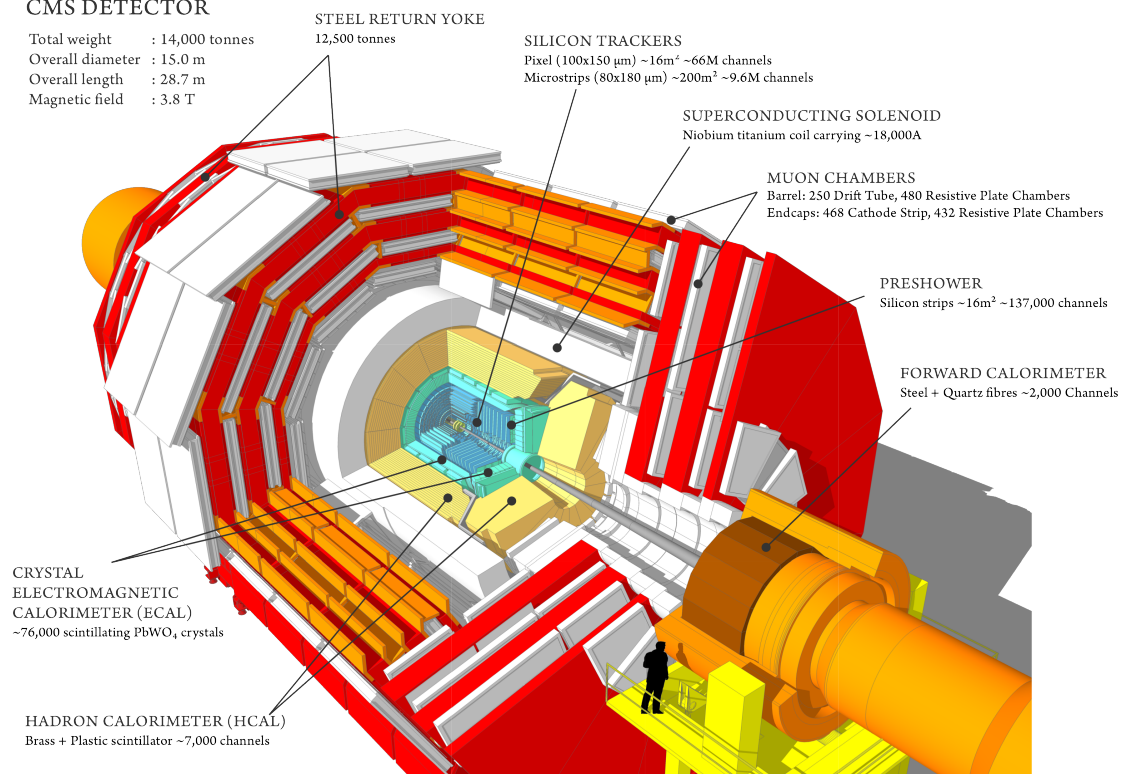


Figure 1: *Scheme of the CMS detector at CERN with the pixel detector in its centre [3]*



## 2 CMS pixel detector

The current pixel detector consists of a central part, the barrel detector which is a cylinder around the beam line that has three sensitive layers for tracking, and of two disks in each end cap which are perpendicular to the beam line. The layers are made of components called modules which have a silicon sensor. When charged particles interact with the sensor, they create charge which is detected by readout chips (ROCs). Each module holds 16 ROCs. The pixel detector measures the trajectory of charged particles. The particle's tracks are curved by the magnetic field created by the solenoid, and by measuring the radius of curvature the particle's momentum can be determined.

With the new LHC run starting in 2015, the centre of mass energy of the collisions is expected to reach 13 TeV [5]. Furthermore, both the luminosity and the frequency of the proton bunches will increase by almost a factor two [7]. This will increase the number of events as well as their complexity. Therefore, the efficiency of the pixel detector will be limited mostly by its readout speed. Another problem is that the current detector will suffer from radiation damage such as defects in the silicon crystals created when highly energetic particles hit the silicon sensors and the ROCs. This is why an upgraded version of the CMS pixel detector is planned to be installed in 2016/2017. The main difference to the current one is that it will use newly developed ROCs and that a layer of modules is added in both the barrel part and in each of the end caps (Figure 6). The layers of the upgraded barrel detector are placed at radii of 30 mm to 160 mm from the beam line [7]. Since the new detector has one additional layer of modules and because the innermost layer is closer to the interaction point where the collisions occur compared to the current version, it will improve the precision with which the path of particles can be reconstructed. The upgraded pixel detector will be able to work efficiently at luminosities up to  $2 \times 10^{34} \text{ cm}^{-2} \text{ s}^{-1}$  [13].

The pixel detector is a semiconductor detector. Its sensor consists of silicon, which has two distinct regions. The p region is doped with a material that creates an excess of electrons in this part of the silicon, and the n region is doped with another material that leads to an excess of so called holes, which can be considered as positive charges. This is called a p-n junction. It creates a charge diffusion at the interface that leads to a depletion zone which is a region without any free charge carriers. It is created by the recombination of diffusing electron and holes between both blocks next to the interface, thus creating a potential barrier that cannot be crossed by charge carriers any more. The depletion zone can be broadened by applying a reverse bias. Hence, without any particle interaction, there is a zone without any free charge carriers in the sensor. If it is hit by a charged particle, electron-hole pairs are produced resulting in a charge which is not confounded with intrinsic charges in the silicon and is collected by the applied electric field and read

out by the ROC. More information about p-n junctions can be found in [21].

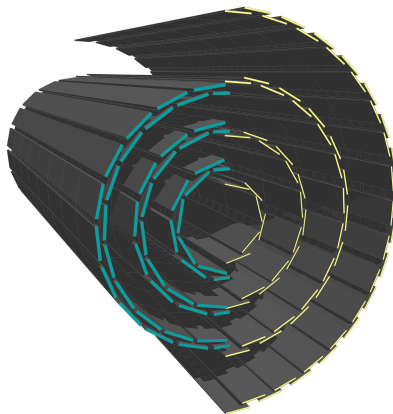


Figure 2: *Scheme of the barrel part of the silicon pixel detector of CMS (Original version - left ; Upgrade - right) A fourth layer is added in the updated version, and the innermost layer is closer to the beam line [6].*

## 2.1 The CMS readout chip (ROC)

The upgraded version of the pixel detector will use a new version of ROCs which differs from the current analog ones mostly due to their digital readout. Each ROC has 4160 pixel unit cells (PUC) each of which consists of readout electronics which are connected to the silicon sensor of the module with metal bumps. The size of a PUC is  $100 \cdot 150 \mu\text{m}$  while ROCs measure  $7.9 \cdot 10.2 \text{ mm}$  [7].

There are 16 digital-to-analog converters (DACs) that can be configured for each ROC. Those parameters are either set globally for the entire module, or one by one for individual ROCs.

Every ROC is divided in three parts as can be seen in Figure 3. The first one is the pixel array, consisting of the PUCs arranged in 80 rows and 26 double columns. The PUCs detect the charge produced by particles crossing the silicon sensor, amplify and shape the signal and compare it to a threshold which is set with the  $V_{thrComp}$  and  $V_{trim}$  DACs. Each double column is linked to an interface (DCI) which reads out the signal and stores it. The DCI was modified for the new ROC generation because at higher luminosities, more data will have to be stored in the data buffers. Therefore, more data and timestamp buffers are added, which makes the digital ROCs slightly larger than the current analog ones. Furthermore, to reduce the dead-time of a double column during the ROC readout, an additional readout buffer is included in the ROC. The data from each double column is combined in the control interface block (CIB) that organizes the double-columns readout. The CIB has an 8 bit analog-to-digital converter (ADC) which transforms the charge produced in a pixel in a digital signal which can be read at 160 MBit/s [13]. Figure 4 shows the

different elements of the readout chain while Figure 5 shows the data format of the ROC readout including the row and column of the pixel that detected an incoming charge as well as the pulse height [12].

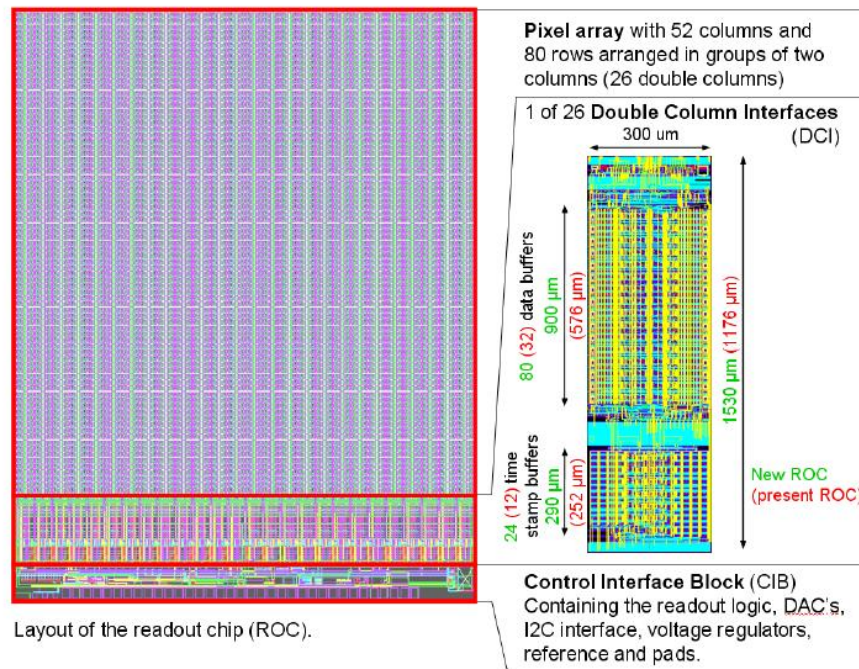


Figure 3: *Structure of a ROC. It consists of a pixel array, 26 double column interfaces which read and store signals from the double columns, and a CIB that controls the readout of the ROC [13]*

## 2.2 Pixel detector modules

The modules for the upgraded pixel detector will have two rows of eight ROCs, therefore there will be 66560 PUCs in each module (4160 per ROC) [7].

Figure 6 shows the different components of the new modules. From bottom to top, the modules for layers 2-4 consist of base strips for fixation, the 16 ROCs, a silicon sensor, and an HDI (High Density Interconnect) which provides a link between the ROCs and the TBM (Token Bit Manager Chip) that regulates the readout from all ROCs. A cable combining power supply for the module and signal output is attached to each module. Layer 1 type modules differ by the way they will be installed in the new pixel detector. Since the circumference of the first layer is too small to fix the modules with base strips, they will be mounted with carbon fibre clips instead [7]. Furthermore, layer one modules also have a dedicated chip design. While layer two to four modules have only one TBM and therefore one data stream out of the module, layer one modules have two TBMs and thus two data links to

increase the readout speed [13]. This is important because layer one is closest to the interaction vertex and therefore has a higher hit rate than the other layers.

### 2.3 Energy calibration

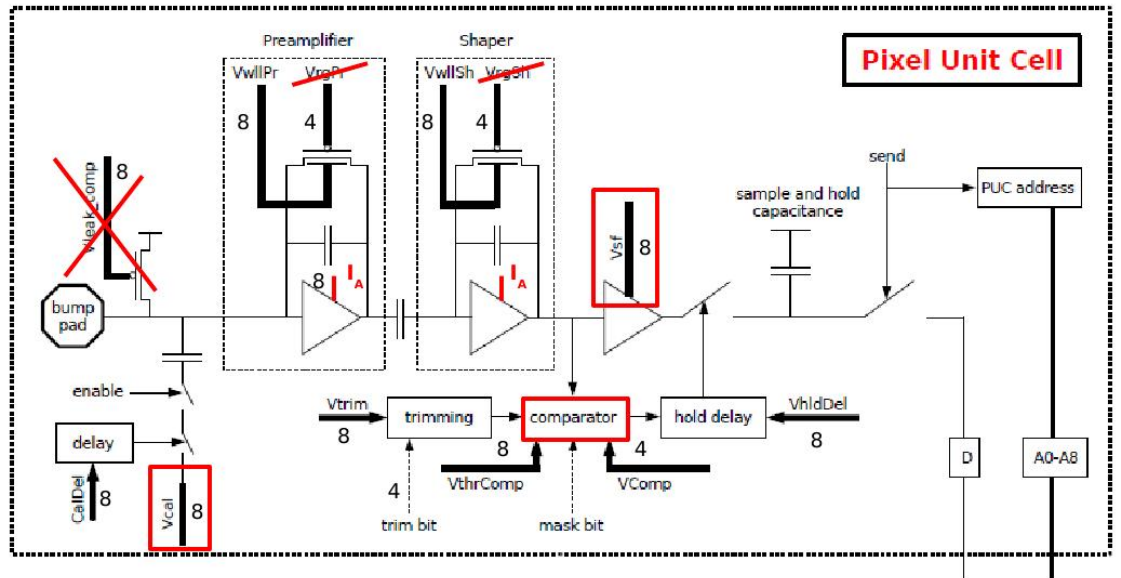
In order to compare the output signal of the detector with the initial charge in the sensor, every module is calibrated before it is installed in the pixel detector. The calibration is done with photons instead of charged particles because for photons, it is possible to know the exact energy that is deposited in the sensor. This is because photons are either absorbed by the sensor depositing all their energy or they do not interact with it all.

A photon that is detected by the pixel detector creates several thousand electron-hole pairs in the silicon sensor by photoelectric effect. Since 3.6 eV are needed to produce one electron-hole pair in silicon, the total number of produced pairs is proportional to the energy of the incoming photon as can be drawn from the following relation, where  $N$  is the number of electron-hole pairs and  $E$  the energy of the incident photon [19]:

$$N = \frac{E}{3.6 \text{ eV}}. \quad (1)$$

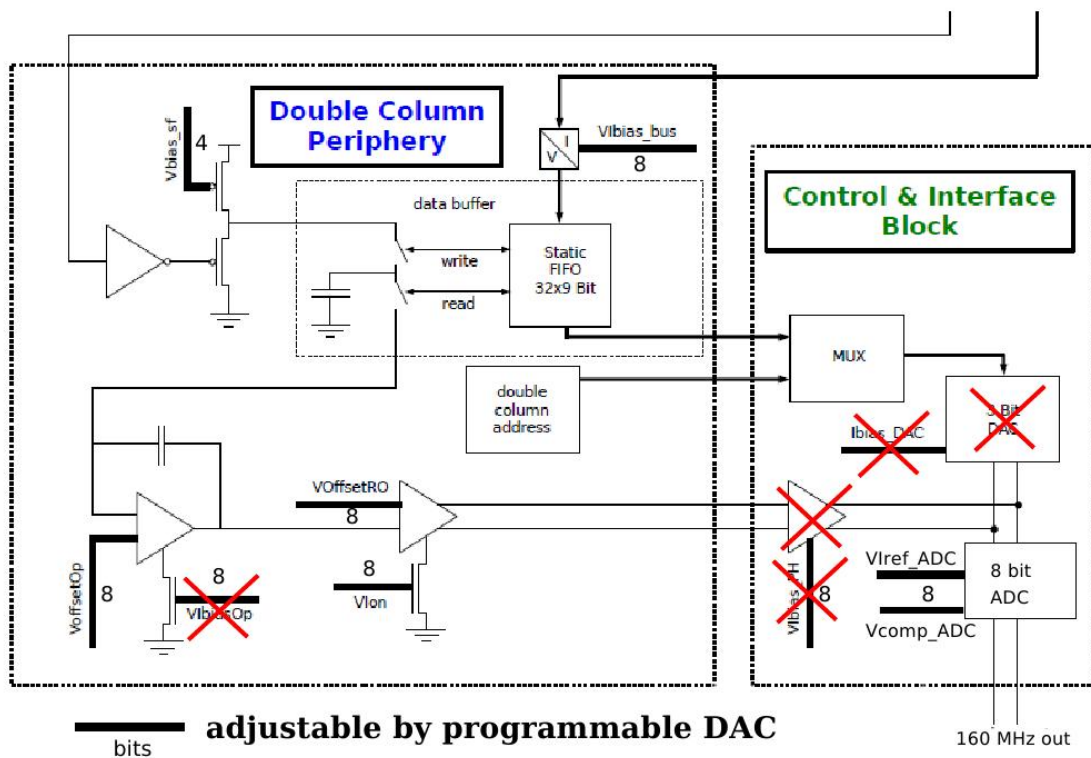
For the calibration, a *PHCalibration* which connects a Vcal value to a pulse height of a signal is carried out first. During a *PHCalibration*, incoming charges are simulated by the injection of Vcal pulses. The pulses are injected to the PUC and are then going through the readout chain shown in Figure 4 and are converted to a pulse height, which is the ADC value read out from the detector. An example of a *PHCalibration* can be found in Figure 8.

For a Vcal calibration, the detector is irradiated with X-rays coming from the excitation of a target material whose emission spectrum is precisely known. The incoming charge is converted to an ADC value in the readout chain. This pulse height can then be converted into the corresponding Vcal value with the data from the *PHCalibration*. The Vcal value of every hit is entered in a histogram and this way the energy spectrum can be measured with a module. Its peak can be fitted with a Gaussian whose mean gives the Vcal value corresponding to the energy of the incoming photons. Therefore, it is possible to connect a number of electron-holes pairs produced by an incoming particle in the silicon sensor to a Vcal value. More information about this and another method to carry out a Vcal calibration can be found in [14].



— bits adjustable by programmable DAC

□ modified in psi46dig



— bits adjustable by programmable DAC

160 MHz out

Figure 4: Scheme of the readout chain for the digital ROC. An incoming particle produces a charge in the silicon sensor which is transmitted to the readout electronics of the PUC by the bump pad. The signal is then amplified and shaped. If the signal is above the threshold set with the  $V_{thrComp}$  and  $V_{trim}$  DACs, it is transferred to the double column periphery where it is stored before being converted to a digital signal in the CIB. [12]

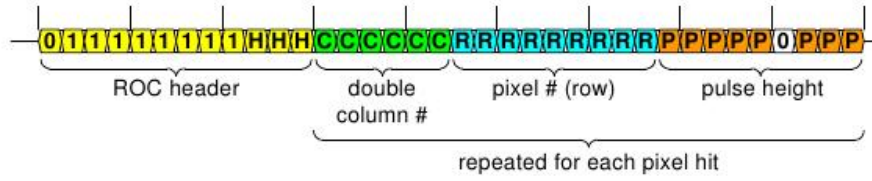


Figure 5: *The readout signal of a digital ROC encodes the number of the ROC that detected the hit as well as the number of the corresponding column, the pixel number and the pulse height [12].*

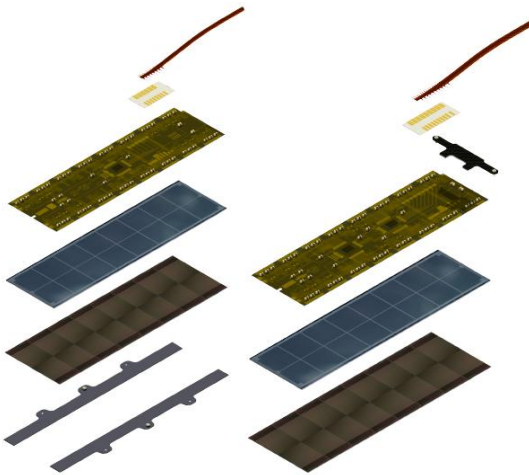


Figure 6: *Modules for the Pixel Detector Upgrade: Layer 2-4 (left); Layer 1 (right). From bottom to top, modules are made of base strips for fixation, 16 ROCs, a silicon sensor, an HDI, a TBM and a shared cable for signal and power[7].*

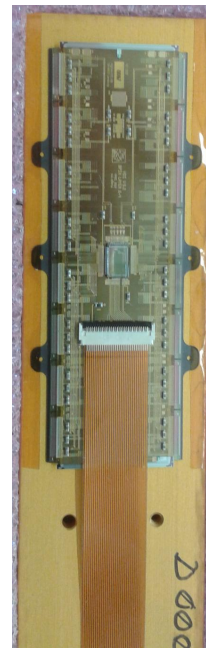


Figure 7: *Photograph of a digital module on a module holder which shows the different components of the module such as the TBM, the HDI and the shared cable for power and signal.*

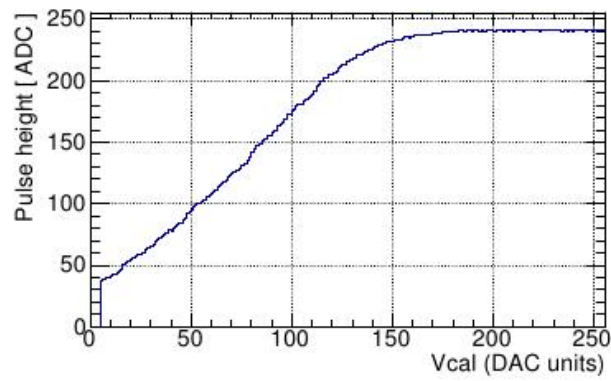


Figure 8: *Example of a PHCalibration which gives the relation between Vcal values and ADC units. The pulse height increases linearly with Vcal values up to around 120 Vcal and then saturates. The energy deposited by charged particles in the sensor during the experiment is in the Vcal range where the pulse height varies linearly [15].*

### 3 Measurements of the X-radiation with spectrometer

As explained in the previous section, it is essential to perform a Vcal calibration on ROCs in every module before using them in the CMS pixel detector. For this calibration, they are irradiated with X-rays with a precisely known energy in a setup. The aim of this section will be to study the properties of the X-radiation in the available setup and to test how it could be optimized.

#### 3.1 X-ray setup for module calibration

The setup for Vcal calibrations of ROCs consists of an X-ray source that produces a beam that can be either used directly, or to produce secondary emission by interaction with one of seven different target materials (Figure 9). Filters are available for four of the target materials. Furthermore, single chip modules or entire modules can be fixed in a test setup underneath the X-ray source for measurements.

The data taken with ROCs or modules is analysed with a software named pyXar written in python which was created by the ETH pixel group. Multiple tests are implemented in this software. The ones used for this work are:

- *Calibrate* which tests if all pixels are working
- *Trim* which sets the threshold of the comparator by optimizing the values for the VthrComp and Vtrim DACs as well as the trimbits for each pixel. In the following all ROCs were trimmed to Vcal 40.
- *PHCalibration* which connects a pulse height from a hit pixel to a Vcal value
- *HRMap* that produces a hit map which is a map that gives the number of hits in each pixel. It also gives the energy spectrum which is used for a Vcal calibration.

The X-ray source that was used is a Seifert X-ray tube which has a chromium (Cr) anode. X-rays are generated by accelerated electrons which collide with the anode, hence creating bremsstrahlung. The photons hereby produced are in the X-ray range with a wavelength between 0.01 and 10 nm.

As stated before, monochromatic X-rays can be obtained by secondary emission. This is produced when high energy X-rays interact with a target material by kicking out electrons from the inner orbitals of the atoms. To minimize each atom's internal energy, electrons from higher orbitals occupy the ones from the electrons that have been removed by the photons. The energy the atom loses this way is carried by a photon. This leads to a spectrum with precise energy peaks due to the fact that for





Figure 9: *Picture of the X-ray source on the right and the target holder with the seven different target materials on the left. The target holder can be moved such that every target material can be placed in front of the X-ray source.*

each material, there are specific energies at which photons can be emitted. These will be used as reference energies for the calibration of modules as explained in section 2.3. Typically, both the  $K_\alpha$  which is made of photons emitted by electrons going from a 2p state to the 1s state of an atom and the  $K_\beta$  lines can be observed in the spectrum. The  $K_\beta$  line is created by electrons going from a 3p state to the 1s state. The target materials which are available are Iron (Fe), Copper (Cu), Bromine (Br), Molybdenum (Mo), Silver (Ag), Tin (Sn) and Barium (Ba).

It is also possible to use filters to modify the spectrum that is obtained by secondary emission from the targets. The aim is to remove the  $K_\beta$  line, such that only the  $K_\alpha$  line remains in the spectrum. The filters were put in the holder that is shown in Figure 10.

### 3.2 Spectrometer X-123 from Amptek

To analyse the fluorescence coming from the different target materials, a X-123 spectrometer from Amptek has been used. Its optimum energy range is between 1 and 40 keV. To ensure that it is in its working range, the X-rays power should not exceed 120 W [11]. For a more detailed description of this device, see [9].

### 3.3 X-ray spectra measured with spectrometer

As described above, two types of emissions can be obtained from the setup, the primary beam is the one coming directly from the X-ray source and the secondary

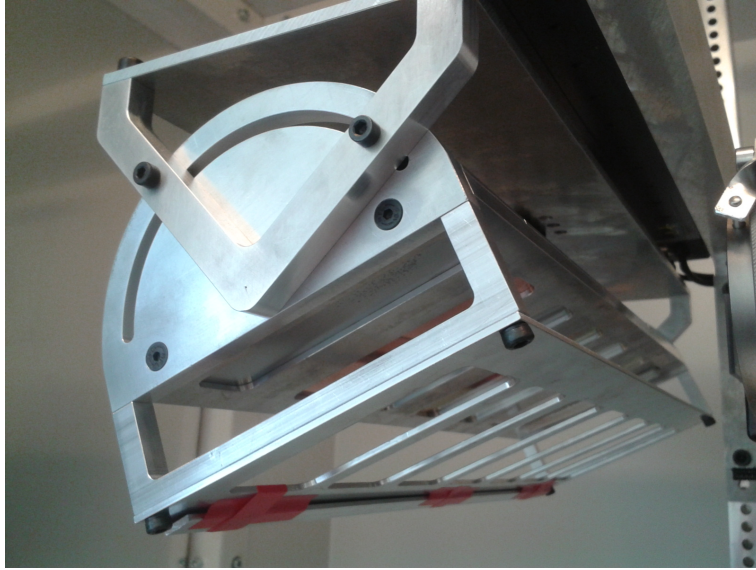


Figure 10: *Picture of the filter holder which is screwed onto the target holder.*

emission is created by the interaction of the primary X-ray beam with the target materials.

The spectra obtained via secondary emission from all target materials (Fe, Cu, Br, Mo, Ag, Sn, Ba) were measured with the spectrometer at different positions in the box. This is done to test if the secondary emission is isotropic. In the following, they will be referred to as left front (LF), left back (LB), right front (RF), right back (RB) and centre (C) as shown in Figure 11.

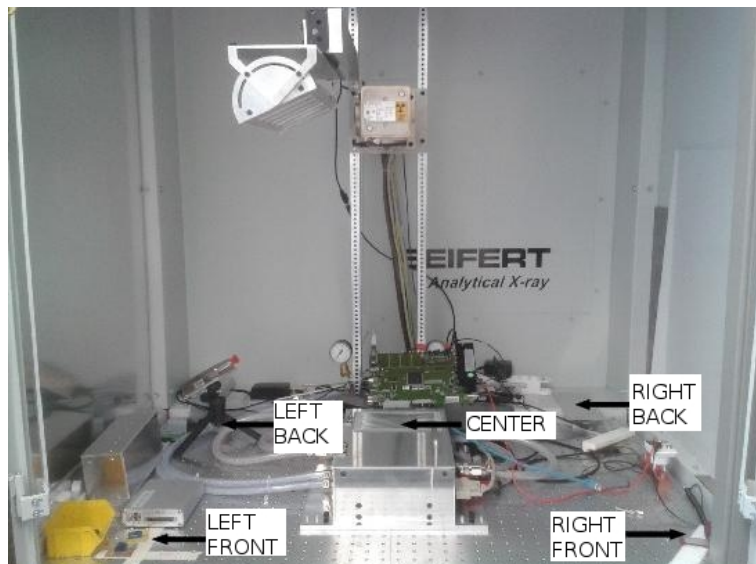


Figure 11: *Different positions of the spectrometer for measurements. Five positions are defined: left front (LF), left back (LB), right front (RF), right back (RB) and centre (C) which are at each corner of the box as well as on top of the test setup.*

For the following results, unless otherwise specified, data was taken during 60 s, with a gain of 24. The spectrometer assigns a channel number to each incoming photon which is related to its energy by the gain. Therefore, the gain determines the energy range that is covered. The tube current was 2 mA and the applied voltage between cathode and anode was 60 kV. These settings were used to ensure that the produced X-rays are in the working range of the spectrometer. If the count rate is too high, it is not able to work correctly, and will show an incorrect result and might be damaged.

All spectra presented in the following sections were calibrated meaning that the channel number was converted to an energy. This was done using the  $K_\alpha$  line of the Fe and Ba spectra for which the energies were looked up in [10]. Furthermore, the intensity of the spectra was corrected for the efficiency of the spectrometer since it is not constant for the entire energy range covered. For this, the data converter written by D. Villar which can be found in the appendix of [9] was used.

### 3.3.1 Isotropy of the X-ray illumination

First, the isotropy of the X-radiation has been studied.

The spectra obtained in the four corners of the X-ray box can be seen in Figure 12 for the LF and LB positions and in Figure 13 for the RF and RB positions. It can be noticed that there is more background in the spectra measured on the left than on the right side. This can be explained by the fact that the primary beam leaves the X-ray source on the left side to interact with the target materials where some photons are only deflected without producing secondary emission. These photons are then also collected by the spectrometer.

Table 1 gives the integral of the  $K_\alpha$  and  $K_\beta$  lines for all target materials at the different positions. The integral is calculated in the range  $[\bar{x} - 3\sigma, \bar{x} + 3\sigma]$ , where  $\bar{x}$  is the mean and  $\sigma$  the standard deviation of the Gaussian that was fitted on the peaks. Several comments can be made here. First of all, the value of the integral and thus the intensity of the radiation is always higher on the left hand side. This can be explained by the fact that the secondary emission from the target materials is normally isotropic [16]. Since the target materials are not in the centre of the box but on the left hand side, when the spectrometer is on the right, it is further away from the secondary emission source than when it is on the left.

It can also be seen that the integral is higher at the front than at the back. This can be explained in the exactly same way, because the "back" positions are further away from the target materials which are the source of the secondary emissions than the positions called front.

For further studies which will be made at the centre of the box and are therefore not so much influenced by variations in the corners, it can be assumed that the

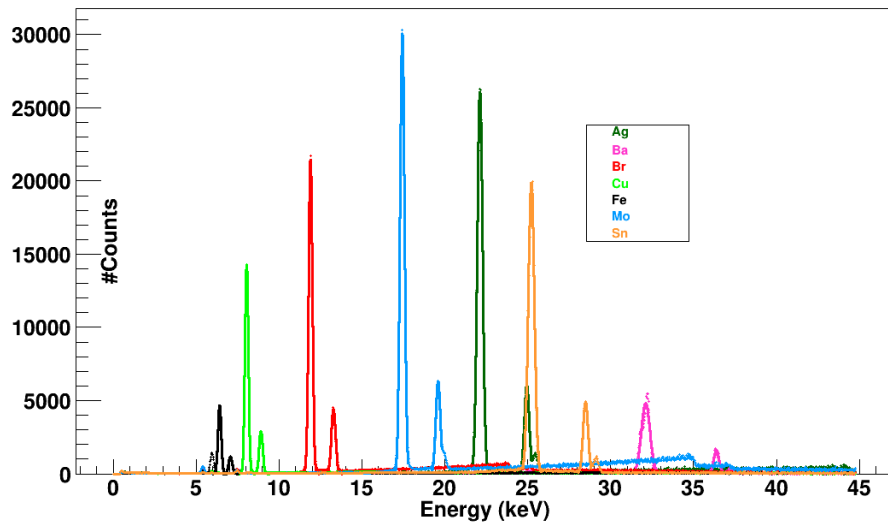
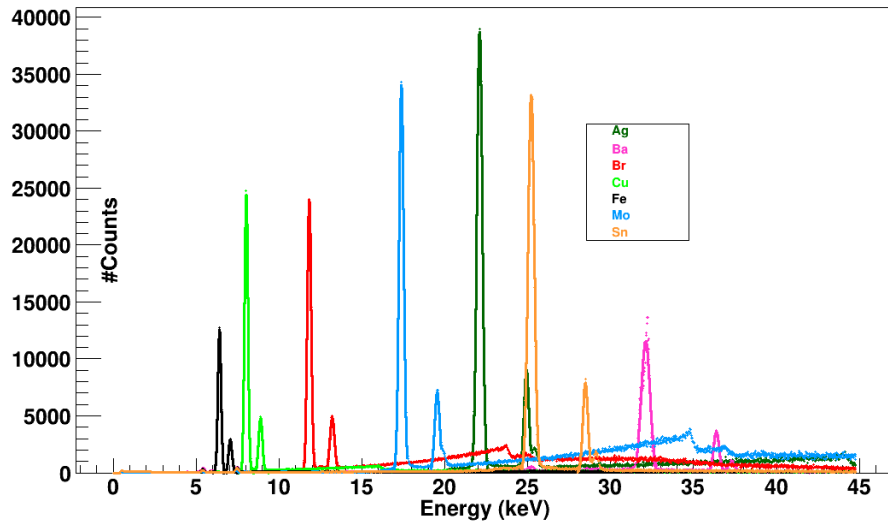


Figure 12: Spectra measured at the left front and left back of the secondary emission from all target materials. For all of them, the  $K_{\alpha}$  and  $K_{\beta}$  emission lines can be seen. The intensity of the secondary emission is higher at LF than at LB. Some background probably coming from X-rays which are deflected by the target materials without creating secondary emission is also observed.

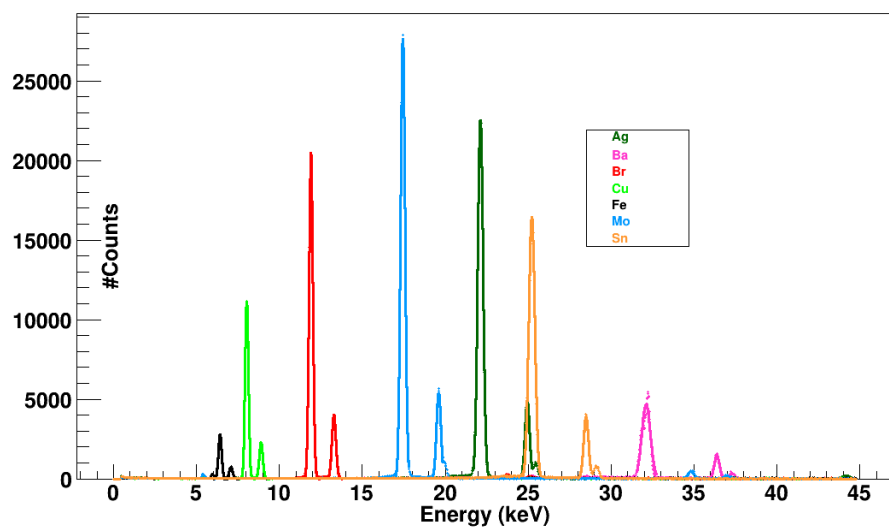
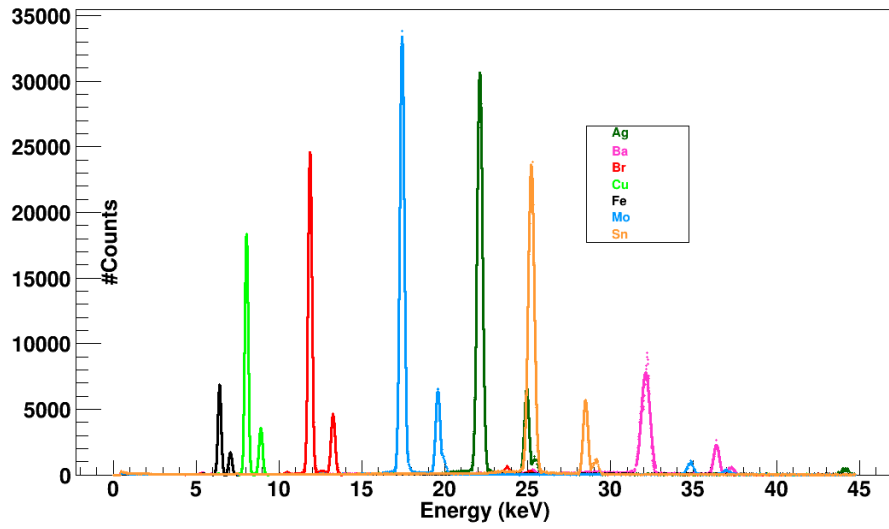


Figure 13: Spectra measured at the right front and right back of the secondary emission from all target materials. Again, both the  $K_{\alpha}$  and  $K_{\beta}$  lines can be seen for every target material. The spectra at RF and RB are similar, however the intensity of the emission is larger at RF. There is less background on the right than on the left side.

intensity of the fluorescence is isotropic and only depends on the distance to the secondary emission source.

For a Vcal calibration, it is important that the energy of the  $K_\alpha$  line is independent from the position of the module. Table 2 gives for all seven target materials the energy of the main peak ( $K_\alpha$ ) measured by the spectrometer on positions RF, RB, LF and LB. For all tests, it can be seen that the energy of this line is in good agreement with the theoretical values found in tables such as in [10]. This indicates that the measured values are correct and shows that the energy of the monochromatic x-radiation is isotropic.

Table 1: *Integral of the  $K_\alpha$  and  $K_\beta$  peaks for all target materials at different positions. The intensity of the emission lines is highest at the LF position, RB has the lowest intensity. This is due to different distances of the spectrometer to the target materials which are the source of the secondary emission.*

Targets	LF		LB		RF		RB	
	$K_\alpha$	$K_\beta$	$K_\alpha$	$K_\beta$	$K_\alpha$	$K_\beta$	$K_\alpha$	$K_\beta$
Fe	3,017	758	1,138	311	1,643	423	665	190
Cu	6,227	1,353	3,595	788	4,611	939	2,777	601
Br	7,033	1,712	6,061	1,398	7,034	1,414	5,769	1,208
Mo	11,875	2,941	10,030	2,364	11,268	2,290	9,191	1,862
Ag	15,689	3,531	10,387	2,265	12,242	2,328	8,914	1,716
Sn	15,369	3,025	9,029	1,854	10,726	2,041	7,472	1,439
Ba	7,062	1,514	2,919	649	4,781	948	2,880	569

### 3.3.2 Background reduction with filters

Most importantly, the spectrum must be well known in the centre because this is where single chip modules or entire modules will be tested. In this section, it will be studied if X-radiation is modified when crossing an aluminium foil and if filters modify the spectra obtained with a spectrometer.

#### 3.3.2.1 Spectrum in the centre

ROCs or modules are shielded by an aluminium foil during measurements to avoid large leakage currents. Therefore, the spectrum was measured twice at the centre, once with an aluminium foil covering the spectrometer and once without to test if the foil also has an impact on the X-rays.

Table 2: *Energy of the  $K_\alpha$  line in keV for all materials at different positions of the spectrometer. For all positions, the energy of the  $K_\alpha$  lines of all target materials are very close to the theoretical values.*

Element	Theoretical	RF	RB	LF	LB
Fe	6.40	6.4	6.4	6.4	6.4
Cu	8.05	8.0	8.0	8.0	8.0
Br	11.92	11.9	11.9	11.8	11.9
Mo	17.48	17.4	17.4	17.4	17.4
Ag	22.16	22.1	22.1	22.1	22.1
Sn	25.27	25.3	25.2	25.2	25.2
Ba	32.19	32.2	32.2	32.2	32.2

Figure 14 shows the spectra in the centre for all target materials without aluminium foil covering the spectrometer and Figure 15 show the same but this time with an aluminium foil. A noteworthy difference between them can be seen in Table 3. The integral of both the  $K_\alpha$  and the  $K_\beta$  lines are not identical for the two scenarios. For lighter target materials (Fe and Cu), it is slightly smaller when the X-rays passed the aluminium foil than if it did not. This is expected since the aluminium foil stops part of the X-rays. For all other target materials, the intensity slightly increases when the aluminium foil is placed on the spectrometer. One possible explanation for this unexpected result is that without the aluminium foil, the intensity of the X-ray beam is too high such that the spectrometer does not count all the incoming photons.

As done previously for the different positions of the spectrometer, the energy of the  $K_\alpha$  line of the spectra is compared to the reference values in [10]. As expected, it can be seen in Table 4 that for all seven target materials, the aluminium foil does not have a significant impact on the energy of the  $K_\alpha$  line and that the measured values agree well with the expected ones. This is more important for Vcal calibrations of modules than whether the intensity of the radiation is modified by crossing the foil.

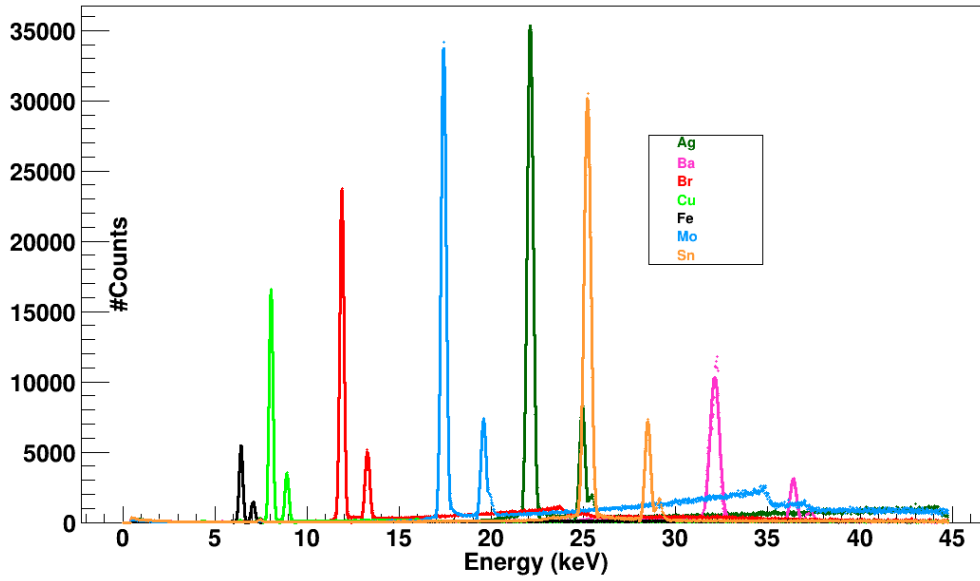


Figure 14: *Spectrum of the secondary emissions of all targets measured in the centre. The intensities of the emission lines are slightly larger than on the right side because in the centre the spectrometer is closer to the target materials than when it is on the RB or RF positions. As on the left side, some background can be observed.*

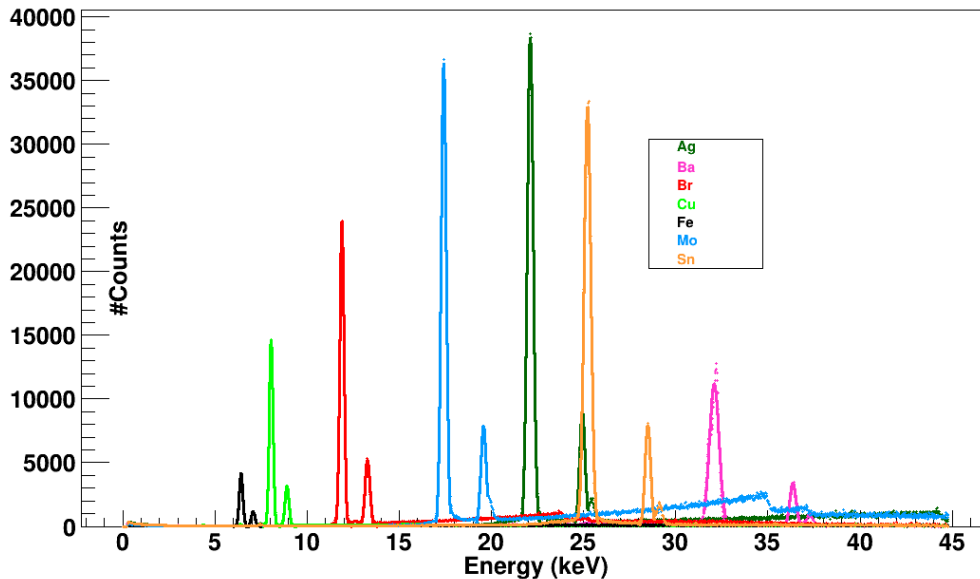


Figure 15: *Spectrum of the secondary emissions of all targets after crossing an aluminium foil measured in the centre. Crossing an aluminium foil influences the intensity of the energy peaks. For Fe and Cu targets, the foil reduces the intensity, for the other target materials, the intensity increases. This might be due to the fact that the intensity without the aluminium foil is slightly too high to be in the working range of the spectrometer such that not all incoming photons are detected.*



Table 3: *Integral of the  $K_\alpha$  and  $K_\beta$  peaks for all target materials with and without aluminium foil on the spectrometer. The value of the integral decreases when X-rays are crossing an aluminium foil for Fe and Cu targets, this is however not the case for all other target materials.*

Targets	With Aluminium		Without Aluminium	
	$K_\alpha$	$K_\beta$	$K_\alpha$	$K_\beta$
Fe	991	300	1,317	372
Cu	3,665	846	4,180	929
Br	6,782	1,697	6,720	1,629
Mo	12,544	3,122	11,667	2,922
Ag	15,537	3,476	14,323	3,183
Sn	15,134	2,989	13,860	2,781
Ba	6,974	1,410	6,213	1,327

Table 4: *Energies of the  $K_\alpha$  line in keV in the centre with an aluminium foil covering the spectrometer and without the foil. The  $K_\alpha$  energy agrees well with the theoretical values and the aluminium foil does not have an impact on the energy of the  $K_\alpha$  line.*

Element	Theor.	C. (with Al)	C. (without Al)
Fe	6.40	6.4	6.4
Cu	8.05	8.0	8.0
Br	11.92	12.0	11.8
Mo	17.48	17.5	17.4
Ag	22.16	22.3	22.1
Sn	25.27	25.4	25.3
Ba	32.19	32.2	32.2

### 3.3.2.2 Influence of filters on the spectra

It will now be studied if filters are able to block the  $K_\beta$  line from the secondary emission. The material that is chosen for the filter is such that its absorption edge is between the  $K_\alpha$  and  $K_\beta$  line energies of the corresponding target material. This is satisfied if the filter element has one or two protons less than the target material [17]. To quantify the effect of filters, two parameters are defined:

- The attenuation coefficient which gives the ratio between the outgoing and the incoming X-ray intensity:

$$K_{i,att} = e^{-\mu_m(E_i) \cdot \rho \cdot t} \quad i = \alpha, \beta \quad (2)$$

where

- $\mu_m(E_i)$  is the energy dependent mass attenuation coefficient for the filter
- $\rho$  is its density and
- $t$  its thickness

- The ratio between the attenuation coefficients of the  $K_\alpha$  and  $K_\beta$  lines:

$$R_{\alpha/\beta} = \frac{K_{\alpha,att}}{K_{\beta,att}} \quad (3)$$

Table 5 gives the choice of filters used here including their thickness and the  $K_{\alpha,att}$  and  $R_{\alpha/\beta}$  coefficients.

For efficient filters,  $K_{\alpha,att}$  should be as close to one as possible which would mean that there is no absorption of the  $K_\alpha$  line. Having a too large absorption would lead to longer measurement times in order to get enough statistics. On the contrary,  $K_{\beta,att}$  should be very small to remove most of the  $K_\beta$  line. Therefore,  $R_{\alpha/\beta}$  should be large.

Filters were available for four different target materials (Cu, Mo, Ag, Sn). Since all filters are very thin, they were left in their card boxes during the measurements to protect them from damage. The measured spectra can be found in Figures 16-19.

For Mo, Ag, and Sn it can be seen that the filters cut away most of the  $K_\beta$  line. The intensity of the  $K_\alpha$  line is reduced by around 50%. The filters also remove part of the background, this is particularly noticeable for Mo. It can also be noticed that the  $K_\alpha$  line of the filter element appears, but its intensity is negligible. On the zoom in Figure 16 these effects can be seen very well. The small peak on the left in the filtered spectra corresponds to the  $K_\alpha$  line from Niobium (Nb).

For Copper, the acquisition time was raised to 5 minutes. Figure 19 shows the spectra with and without filters for Cu as well as the spectrum without filter but where the beam emitted by the Cu target crosses an empty card box before reaching

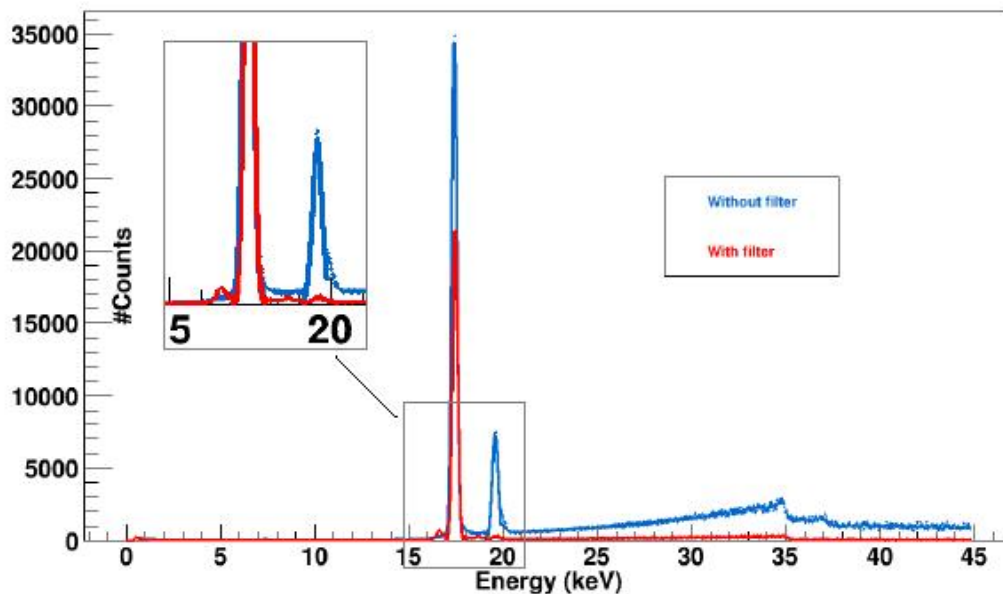


Figure 16: Spectra obtained with and without filters for Mo. The  $K_{\beta}$  peak is almost completely removed and the  $K_{\alpha}$  peak is attenuated. The zoom shows the small contribution from the  $K_{\alpha}$  of the filter material (Nb) on the left and also that most of the  $K_{\beta}$  line is removed.

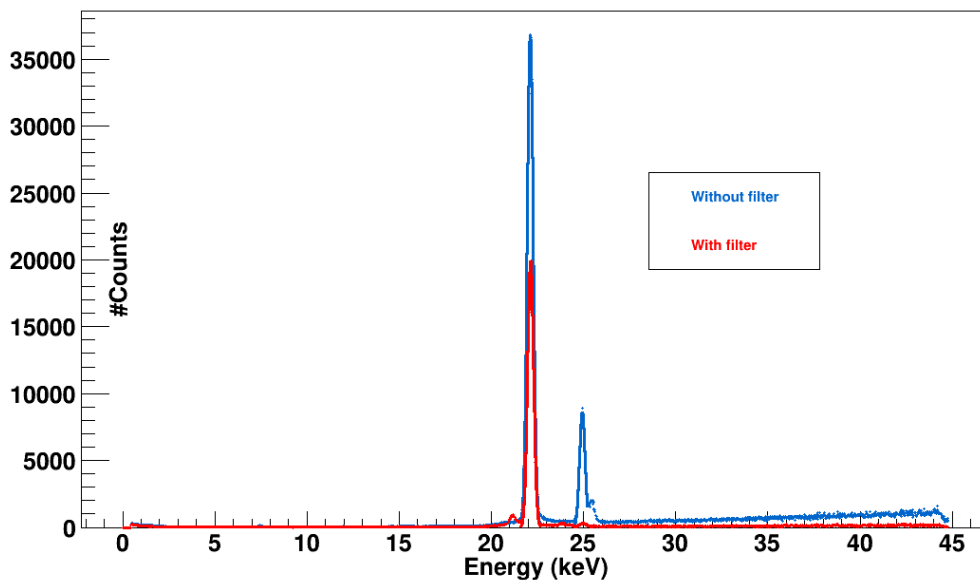


Figure 17: Spectra obtained with and without filters for Ag. The filter blocks almost all X-rays of the  $K_{\beta}$  line and some of the  $K_{\alpha}$  line as well.

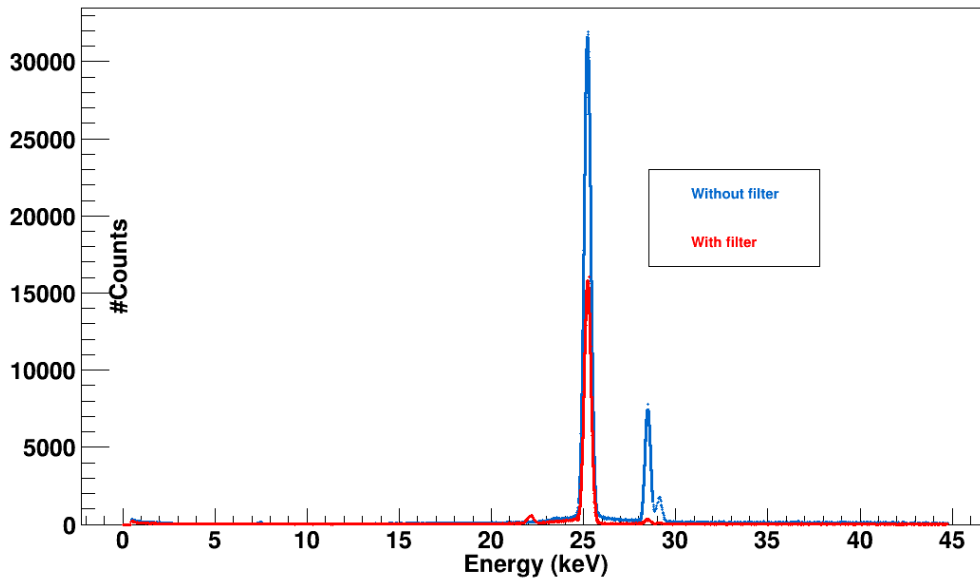


Figure 18: Spectra obtained with and without filters for Sn. The  $K_{\beta}$  line is almost entirely stopped by the filter, while the  $K_{\alpha}$  line is only attenuated by around 50%.

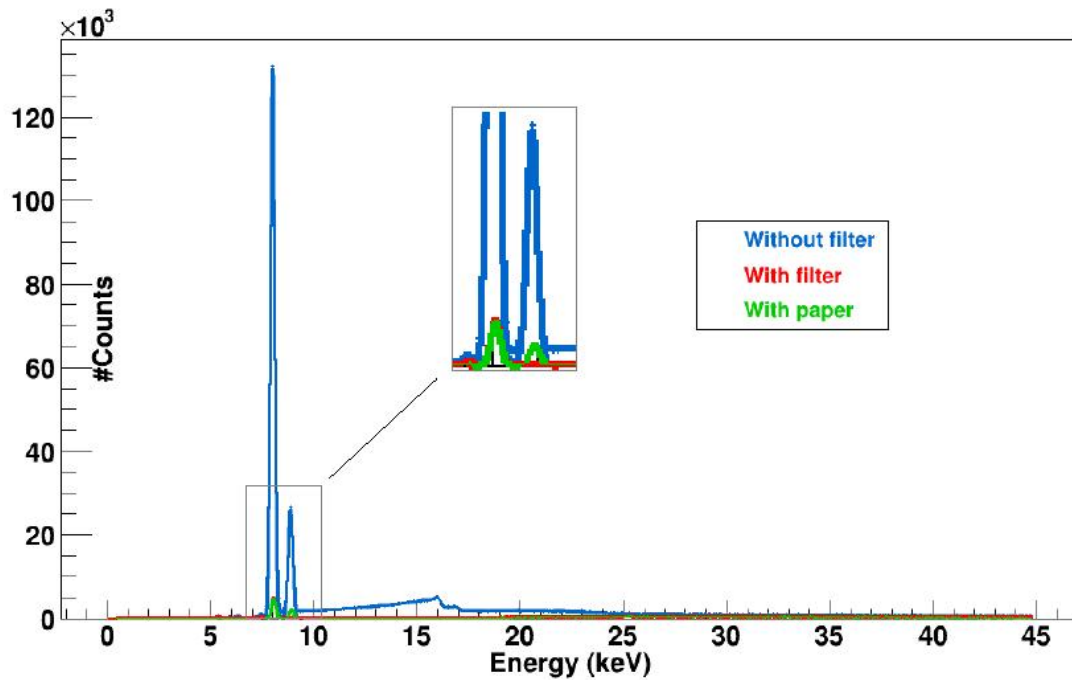


Figure 19: Spectra obtained with and without filters for Cu as well as the spectra of the Cu fluorescence after crossing a card box. The energy of the Cu fluorescence is too small to cross the card box, this is why almost no photons are detected by the spectrometer when a filter is used.

Table 5: *Characteristics of the filters for the Cu, Mo, Ag and Sn targets including their thickness and the  $R_{\alpha/\beta}$  and  $K_{\alpha,att}$  coefficients determined with formulas 2 and 3 which characterize the expected performance of the filters [18].*

Target	Filter	t (mm)	$R_{\alpha/\beta}$	$K_{\alpha,att}$
Cu	Ni	0.015	21.75	0.52
Mo	Nb	0.050	15.13	0.47
Ag	Pd	0.047	11.07	0.48
Sn	Ag	0.075	12.48	0.46

the spectrometer. It can be observed that almost the entire spectrum is suppressed by the card box that protects the filter from damage during the measurement. This is due to the fact that the fluorescence emitted by the Cu target has too little energy to cross the card box. Therefore, in the following only the filters for Mo, Ag, Sn targets will be used to study their influence on Vcal calibrations of modules. If it is found that they improve the calibration, the filter for the Cu target could also be used if taken out of the packaging.

Table 6 compares the experimental results for the values of the  $K_{i,att}$  and  $R_{\alpha/\beta}$  coefficients to the expected values that were given in Table 5. The  $K_{i,att}$  coefficients are determined experimentally as the ratio of the integral of the  $K_i$  line with and without filter. For Mo, Ag and Sn targets, the  $R_{\alpha/\beta}$  coefficient is slightly lower than the expected one in Table 5. The attenuation of the  $K_\alpha$  line on the opposite is higher than expected. This implies that the filters are not removing as much photons from the  $K_\beta$  line as predicted.

Table 6: *Expected values repeated from Table 5 (1) and experimental results (2) for the effect of the filters on the spectra for Mo, Ag and Sn targets. The measured  $R_{\alpha/\beta}$  and  $K_{\alpha,att}$  coefficients are close to the expected values, particularly for Sn and Ag targets.*

Target	Filter	$R_{\alpha/\beta(1)}$	$K_{\alpha,att(1)}$	$R_{\alpha/\beta(2)}$	$K_{\alpha,att(2)}$
Mo	Nb	15.13	0.47	9.88	0.60
Ag	Pd	11.07	0.48	10.2	0.53
Sn	Ag	12.48	0.46	10.2	0.49

These results show that filters have an impact on the spectrum, almost completely removing the  $K_\beta$  emission line of the target material and most of the background

and attenuating the  $K_\alpha$  line by approximately a factor of two. It proves that filters work as expected and that they could potentially lead to beneficial effects on Vcal calibrations of modules for the CMS pixel detector. This will be studied in the next section.

## 4 Impact of filters on Vcal calibration

In the previous section, it was shown that filters modify the spectrum of the monochromatic X-radiation emitted by the target materials. It will now be studied which impact filters have on a Vcal calibration using a single chip module and a full module with 16 ROCs. For this, Mo, Ag and Sn target materials will be used.

### 4.1 Effect of filters on spectra measured with a single chip module

First, the spectrum with and without filter for the three target materials will be measured with the single chip module R0112 (Version PSI46digV2.1). The chosen tube settings were 60 kV and 30 mA and measurements were taken for 100 s. The ROC was trimmed to Vcal 40 and the temperature of the ROC was stabilized at 17°C. Since the chip was not designed to have a perfect energy resolution, the spectra obtained with the single chip module will not have a resolution as good as with the spectrometer. Therefore, the single chip module is not able to distinguish the  $K_\alpha$  and  $K_\beta$  lines which are merged in a wider energy peak which can be observed in the spectrum. It is expected that when using filters, the energy peak which is detected by the single chip module is narrower and the mean of the peak shifted to lower Vcal values due to the fact that filters remove most of the  $K_\beta$  line. The measured spectra with and without filter can be found in Figures 20-22 for the fluorescence of the Mo, Ag and Sn targets. The shoulder on the left side of the peak on all spectra can be explained by the fact that the charge produced in the silicon sensor by an incoming X-ray diffuses in the sensor during the drift and therefore, the charge might be split up over multiple pixels. The spectra with filters were normalized in order to account for the smaller intensity of the X-ray beam. With the addition of a filter, the spectrum for Mo is modified as expected. It can be noticed that the width of the peak is reduced and that it is shifted to lower Vcal values. For Ag and Sn however, the peak of the spectrum with filter is shifted to higher Vcal values. At this point in time no explanation was found for this. While for Ag it can also be observed that the width of the energy peak decreases, no major difference can be seen between both spectra for Sn.

In order to obtain quantitative results for the mean and width of the energy peak, every peak is fitted with a Gaussian over the range  $[\bar{x} - c_1 \cdot r, \bar{x} + c_2 \cdot r]$  where  $\bar{x}$  is the mean energy of the peak,  $r$  is the RMS of the distribution,  $c_{1,2} = \{0.8, 2.2\}$  for Mo,  $c_{1,2} = \{0.7, 1.8\}$  for Ag and  $c_{1,2} = \{0.5, 1.4\}$  for Sn. Examples of fits can be found in Figure 23 while the fits for all 15 measurements are in the appendix. This choice of intervals ensures both that the fit does not take the shoulder on the left side of the peak into account but that it covers the  $K_\beta$  peak at large Vcal values such that the width of the spectrum with and without filters can be compared. The

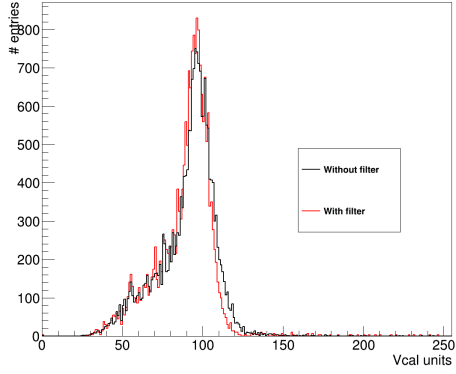


Figure 20: *Mo spectra with and without filters measured with a single chip module. The width of the peak is reduced in the spectrum with filter as expected.*

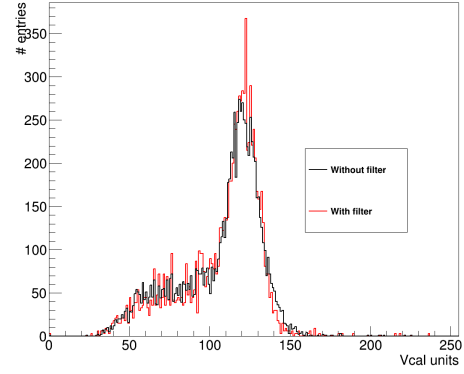


Figure 21: *Ag spectra with and without filters measured with a single chip module. It can be noticed that the width of the spectrum with filter is slightly reduced for Ag as well.*

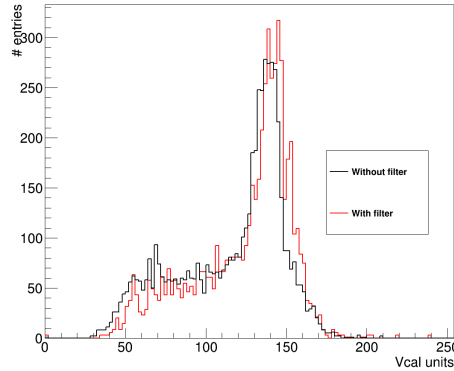


Figure 22: *Sn spectra with and without filters measured by a single chip module. There is no noticeable difference in the width of the energy peak between both spectra, but contrary to what was expected, the mean of the peak is shifted to higher Vcal values when a filter was used.*

value of the  $\sigma$  of the Gaussian fit gives an estimation of the broadness of the peak. Figure 24 shows the value of  $\sigma$  for the fit on the spectra of the three target materials with and without filters. The values given are the average over 15 measurements in order to get more statistics, the error bars are the standard deviation from the mean value of  $\sigma$  (see Figures 65 to 70 in the appendix for separate values for the fifteen measurements). It can be seen that for Mo and Ag,  $\sigma$  decreases by 1.83 Vcal units respectively 1.78 Vcal units while for Sn it increases by 0.05 Vcal units. The results



confirm the observations made on the spectra in the previous paragraph and are as expected for Mo and Ag since they show that filters reduce the width of the energy peak. For Sn however, the filter does not have a significant impact on the width of the energy peak.

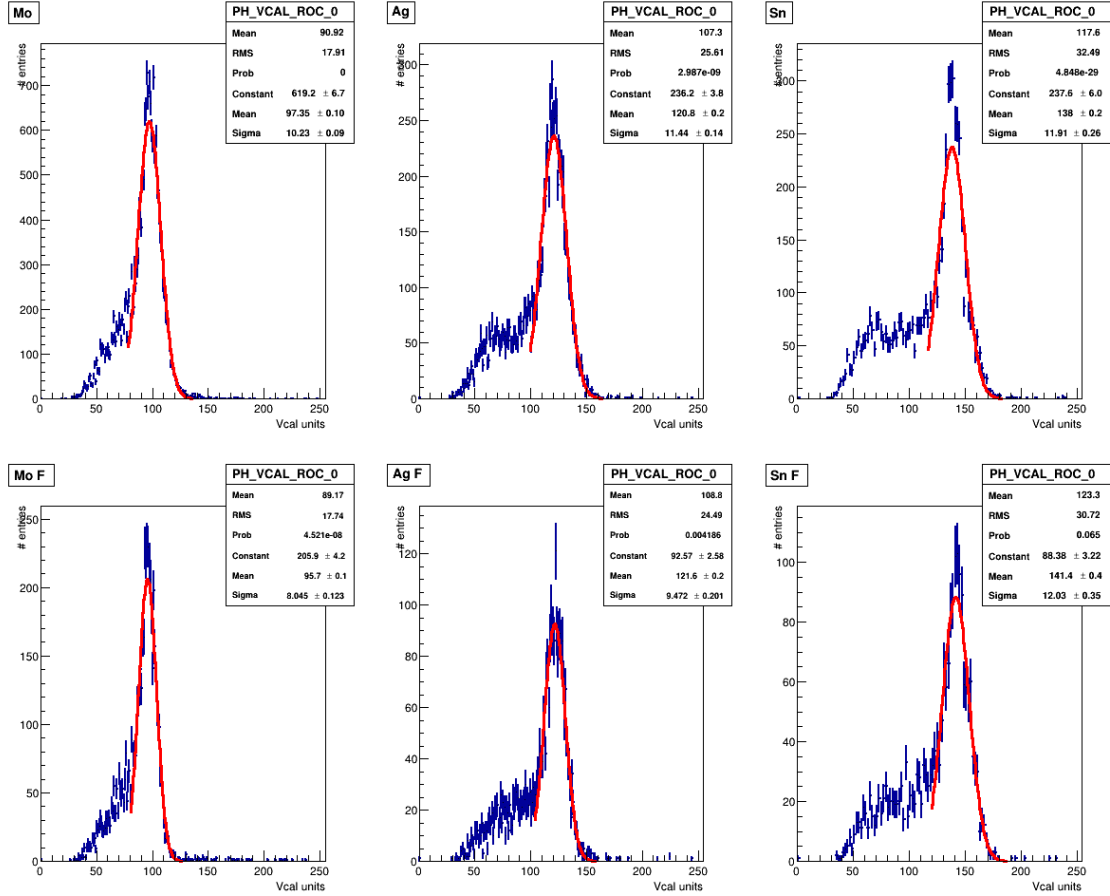


Figure 23: *Examples of fits on the spectra for Mo, Ag and Sn measured with a single chip module. The fits do not cover the shoulder of the peak at lower Vcal values. Top row: Without filter Bottom Row: With filter*

The values for the mean of the peak are also obtained with the Gaussian fit. The average over 15 measurements of the mean of the peak are presented in Figure 25 while the values for the individual measurements can be found in Figures 71 to 76. The errors which are the standard deviation from the average value of the mean on Figure 25 are increased by a factor ten. As explained before, it is expected that the mean of the peak decreases when a filter is added. While for Mo the mean decreases by 1.14 Vcal units, it increases for Ag by 0.15 Vcal units and by 3.87 Vcal units for Sn when filters are used, which is contrary to what is expected. No explanation was found for this to this date therefore this result should be verified in further work.

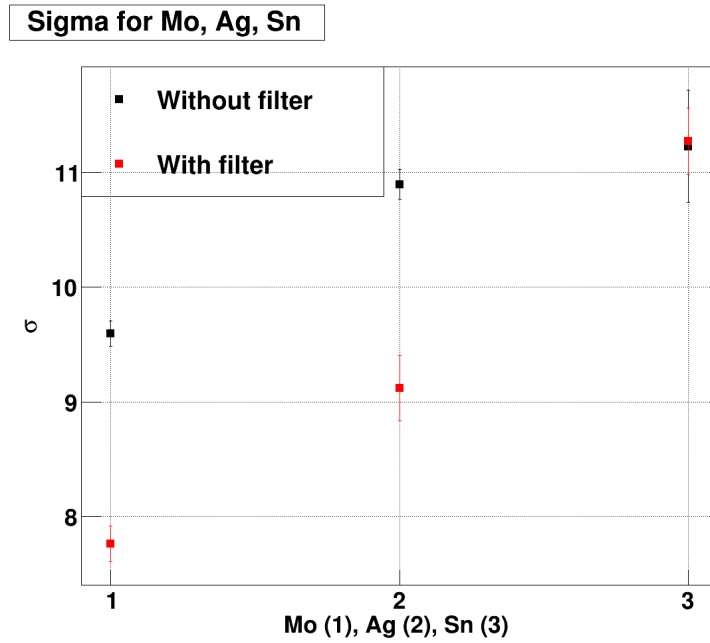


Figure 24: Values for the  $\sigma$  of the Gaussian fit for Mo, Ag and Sn targets with and without filter. It can be noticed that while it decreases for Mo and Ag spectra, filters do not have a significant impact on the width of the peak in the Sn spectrum.

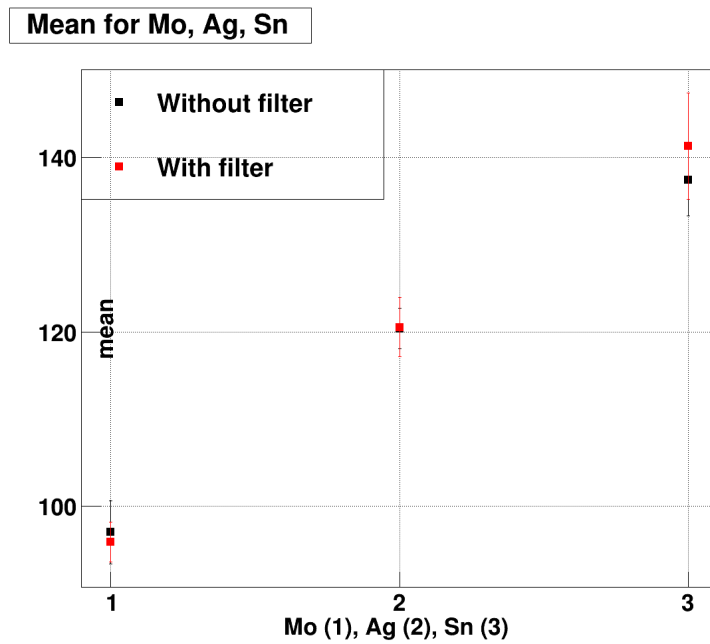


Figure 25: Values for the Mean of the Gaussian fit for Mo, Ag and Sn targets with and without filter. The size of the error bars are increased by a factor ten to make them visible. For Mo, the mean decreases with the addition of a filter as expected. For Ag and Sn however the mean increases, particularly for Sn which is not what was expected.

## 4.2 Effect of filters on the Vcal calibration of a digital read-out chip

A Vcal calibration for the ROC was carried out using the average of the mean over the 15 measurements and taking the standard deviation from the mean as the error on the mean as in the previous section. The results can be found in Figure 26. The slope and offset for the Vcal calibration without filters are  $(54.02 \pm 0.72) e^-/\text{Vcal}$  and  $(-367.4 \pm 85) e^-$ . These results are compatible with the values usually found for a calibration of a digital ROC. When a filter is added, the slope becomes  $(49.94 \pm 0.59) e^-/\text{Vcal}$  and the offset  $(77.6 \pm 64) e^-$ . The slope of the calibration is therefore  $4.1 e^-/\text{Vcal}$  smaller with than without filters. The offset however increases with filters by  $445 e^-$ . It can be noted that the offset is close to zero for the Vcal calibration with filters. Having an offset of zero implies that if no charge is detected by the sensor, then the ROC does not have an output if the linear extrapolation is valid down to Vcal zero. While this seems logical it is at this point neither possible to state whether a correct Vcal calibration should lead to a null offset nor whether filters always lead to a null offset. Furthermore, offsets compatible with zero have already been measured for other ROCs without filters such as for analog ROCs in [9]. It must be noted that the linear fit which gives the values for the slope and the offset is clearly not as good with filters than without. This can be noticed directly on Figure 26 or by comparing the  $\chi^2$  values for the linear fit which are 6.2 without filter and 27.2 with filters. It also has to be remembered that the results for the Vcal calibration with filters are not fully understood because at this point it could not be explained why the energy peak of the Sn spectrum is shifted to higher energies when using filters.

## 4.3 Vcal calibration of a digital module with and without filters

In this section, the results of a Vcal calibration of the digital module D0002 will be presented. The D0002 module has 16 ROCs of version PSI46digV2. The X-ray tube settings and the measurement acquisition time are the same than for the Vcal calibration of the single ROC. ROCs are numbered as shown in Figure 27.

Figure 64 in the appendix shows the Vcal calibration for all ROCs in the module. The peaks in the spectra with filters were fitted with a Gaussian over the range  $[\bar{x} - c_1 \cdot r, \bar{x} + c_2 \cdot r]$  where  $\bar{x}$  is the mean energy of the peak,  $r$  is the RMS of the distribution and in this case  $c_{1,2} = \{0.6, 1.5\}$  for Mo,  $c_{1,2} = \{0.5, 1.2\}$  for Ag and  $c_{1,2} = \{0.4, 1.0\}$  for Sn. The spectra without filter were fitted in the range  $[\bar{x} - c_1 \cdot r, \bar{x} + c_1 \cdot r]$ . It will be explained below why the fit range is symmetric in this case. In Figures 28, 29, 30 and 31, the slope and offset of the Vcal calibration with and without filters are given. The average slope for all ROCs is  $50.2 e^-/\text{Vcal}$

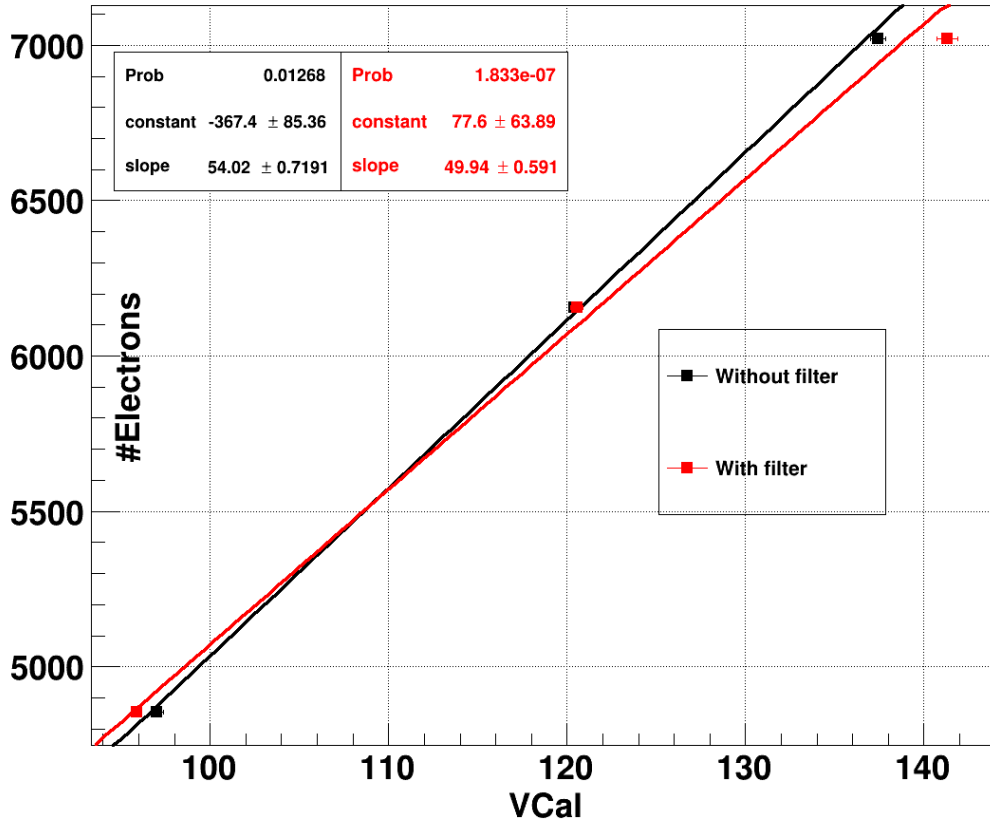


Figure 26: *Vcal* calibration for ROC R0112 with and without filter using Mo, Ag, Sn targets. While the slope is smaller with filter, the offset increases.

without filter and  $50.9 e^-/Vcal$  with filter. The average offset is  $514 e^-$  without filter and  $438 e^-$  with filter. Neither the slope nor the offset of the *Vcal* calibration are significantly modified when a filter is added. Contrary to the results found for the single chip module where the slope decreases by  $4.1 e^-/Vcal$  with filters, the slope only increases by  $0.76 e^-/Vcal$  and the offset decreases by  $76.3 e^-$ , which are of the same order of magnitude than the error on the slope or the offset and are much smaller than the standard deviation of the slope or the offset between the ROCs of the module. For some ROCs such as ROCs 2, 6 and 13, the slope only increases by around  $0.3 e^-/Vcal$  while it increases by more than  $3 e^-/Vcal$  for ROCs 0 and 4 and decreases by  $0.1 e^-/Vcal$  for ROC 3.

It was also studied how good the linear fit on the three points for the *Vcal* calibration is with and without filter. For this, the  $\chi^2$  value was calculated for the fit on the *Vcal* calibration for each ROC in Figures 32 and 33. It can be seen that the mean  $\chi^2$  value of all ROCs is 19.7 without filters and 11.9 with filter. It can be noticed that contrary to what was found for the single chip module the linear fit is better for *Vcal* calibrations with filters than without. For good fits however, the  $\chi^2$

value should be approximately equal to the number of degrees of freedom, which is one in this case. The fact that the  $\chi^2$  values found here are much larger than one can be explained by the fact that the error on the mean of the peak which is generated by the Gaussian fit is very small and probably underestimated for some ROCs.

The fits on the spectra for all ROCs of the module can be found in the appendix. On the Ag and Sn spectra without filter, a smaller second peak can be observed to the right of the main peak. This peak disappears on the spectra with filters, therefore it might be a contribution from the  $K_\beta$  line as is also suggested by Figure 34. It shows the spectra for the Ag fluorescence recorded with the spectrometer and by ROC 11 of the module. The x-axis of the spectrum measured with the spectrometer was recalibrated to convert energy values in keV to Vcal values using the Vcal calibration that was carried out. The number of hits coming from the ROC was multiplied by 100 to get similar count rates for both spectra. The spectrum coming from the ROC was fitted with a Gaussian for each peak. It can be seen that the  $K_\beta$  line measured with the spectrometer is at similar energies than the smaller peak recorded by the ROC which indicated that this peak corresponds to photons of the  $K_\beta$  line. This explains why a smaller fit range has been chosen for the peak of the spectra without filter than with filter for the Vcal calibration because it ensures that the  $K_\beta$  line is not taken into account by the fit. The peak corresponding to the  $K_\beta$  line was not observed for the single chip module. A possible explanation for this is that the *PHCalibration* of the module was more precise and with a more linear pulse height distribution which increases the energy resolution in the spectrum.

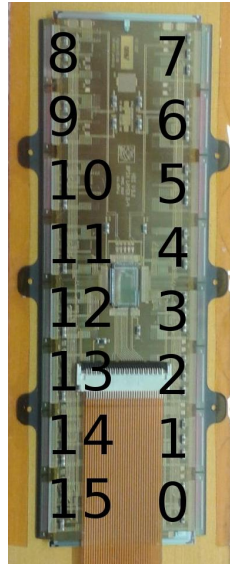


Figure 27: *Numbering of ROCs on the module*

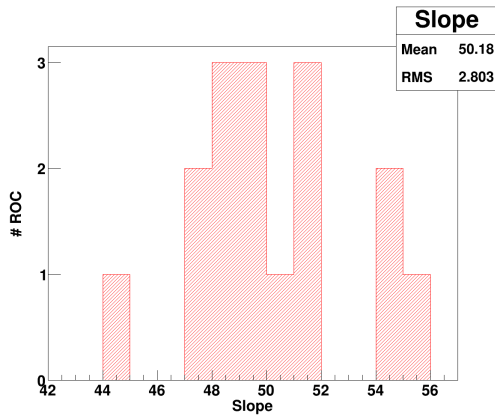


Figure 28: *Slope of the Vcal calibration for all ROCs of a digital module without filter.*

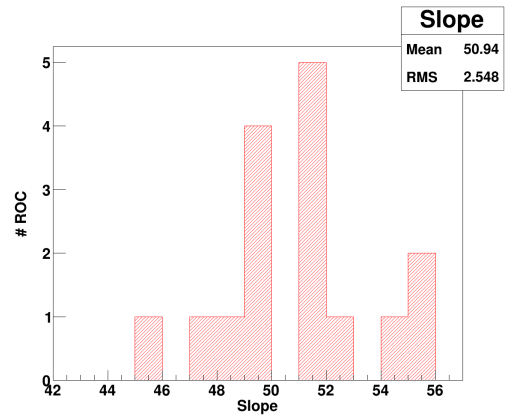


Figure 29: *Slope of the Vcal calibration for all ROCs of a digital module with filter. The mean of the slope for all ROCs is only minimally steeper with filter than without.*

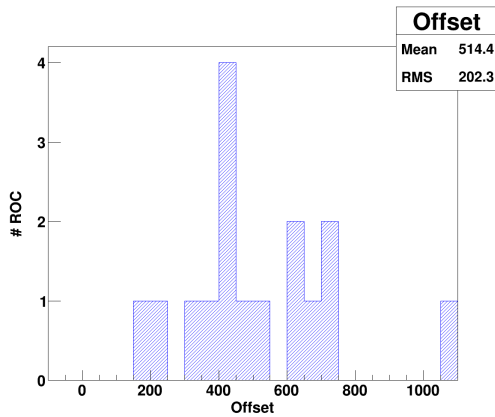


Figure 30: *Offset of the Vcal calibration for all ROCs of a digital module without filter.*

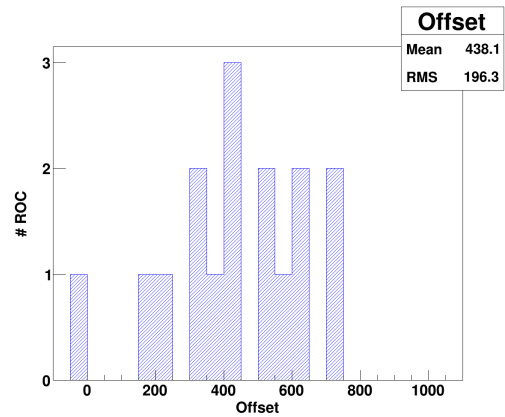


Figure 31: *Offset of the Vcal calibration for all ROCs of a digital module without filter. The mean of the offset for all ROCs is smaller for the Vcal calibration with filters, but the decrease is smaller than the RMS of the distribution.*

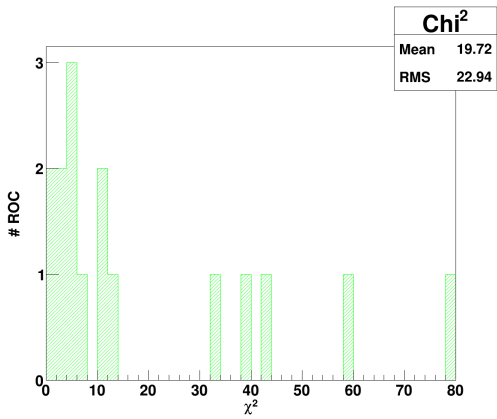


Figure 32:  $\chi^2$  of the *Vcal* calibration for all ROCs of a digital module without filter.

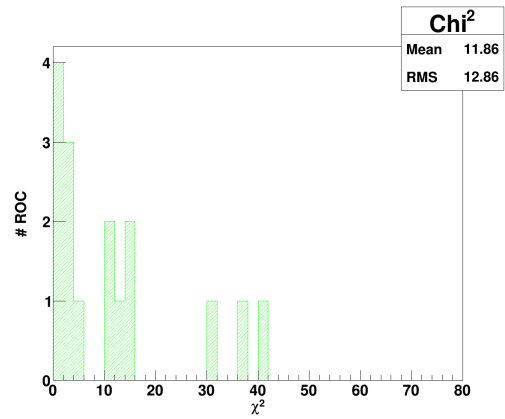


Figure 33:  $\chi^2$  of the *Vcal* calibration for all ROCs of a digital module with filter. The Gaussian fit on the spectra probably underestimates the errors leading to very large  $\chi^2$  values.

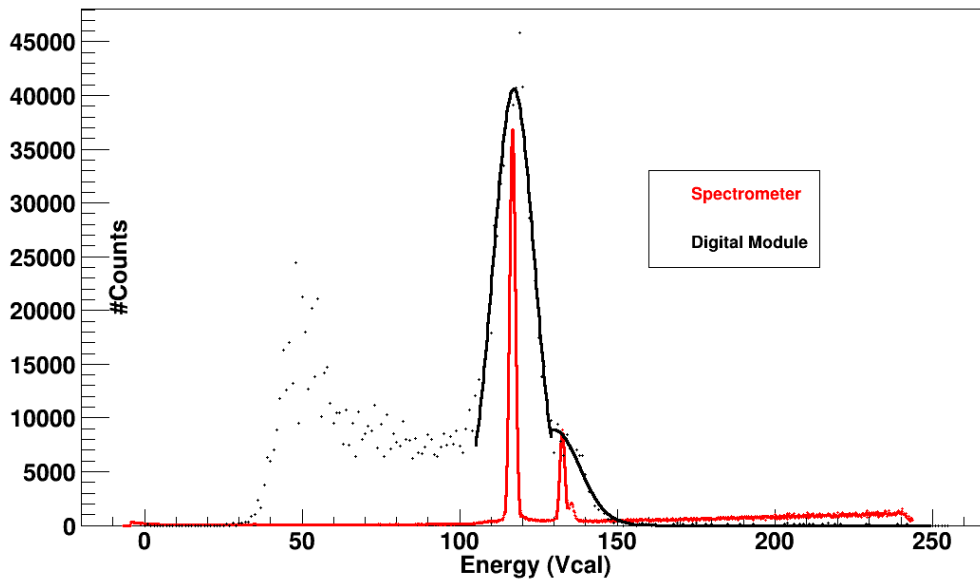


Figure 34: Spectrum recorded by ROC 11 of the module and by the spectrometer of the *Ag* fluorescence. It can be seen that the smaller peak corresponds to the  $K_{\beta}$  line.

## 5 Homogeneity of the X-ray illumination on the module test positions

In this section, it will be studied if the illumination and therefore the hit rate on the module from the primary beam and from the secondary emission coming from target materials is homogeneous on the four available test positions.

The hit rate which is the number of photons detected by the silicon sensor per area and time is given by

$$h_r = \frac{N_{hits}}{A \cdot R_{trigger} \cdot T_{clock} \cdot t} \quad (4)$$

where

- $N_{hits}$  is the number of hits detected by the silicon sensor
- $A$  is the area of the sensor
- $t$  is the data acquisition time
- $R_{trigger} = 31.1$  kHz is the trigger rate and
- $T_{clock} = 25$  ns is the clock time

Some parts of the module are less well illuminated by the X-ray beam than others because the TBM and the HDI are shielding parts of the silicon sensor in some ROCs from incoming radiation. This can be seen in Figure 35 which shows the hit map for the primary beam. A hit map is a map of the module that gives the number of hits in each pixel. The boundaries of individual ROCs can be distinguished because pixels on the edge of the ROCs are twice as large as the other pixels to reduce the inactive area between the ROCs as much as possible. Shadows from the different components of the module which are represented as areas where no hits are collected by the detector can be observed. These shadows are located on pixels in rows zero to 32 of most of the ROCs. These pixels were therefore deactivated during measurements for the following results such that hit rates from different ROCs in the module can be compared without being affected by intrinsic differences created by the shadows. The remaining sensor area is  $0.25 \text{ cm}^2$  per ROC. Noisy pixels were also deactivated so that they do not influence the results. The hit map with masked pixels and rows as described above can be seen in Figure 36. It can be seen that in the region which was not deactivated, the illumination is mostly homogeneous. Therefore it is possible to compare the hit rates on the ROCs of the module.

Figure 37 shows the four test positions of the module. Since only one digital module was available, it was successively tested in all four positions.



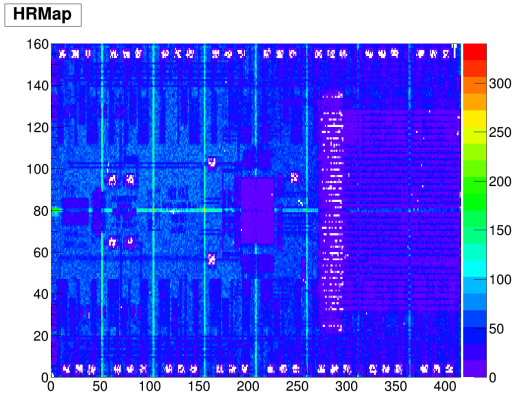


Figure 35: *Hit map from the primary beam without any masked rows. Different components of the module can be distinguished as shadows in regions where no or only few hits were counted. The illumination is mostly homogeneous on all other parts of the module.*

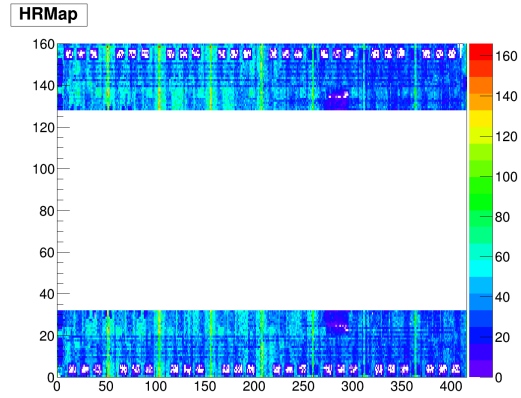


Figure 36: *Hit map from the primary beam where rows 32 to 80 of each ROC were masked. The illumination is more homogeneous except for a little region on ROCs two and 13 where part of the shadow created by the signal and power cable can be seen.*

For the primary beam, data was taken during 3 s and the X-ray tube was set to 30 kV and 5 mA. The hit rates for each ROC of the module on all four test positions can be found in Figure 39. It can be noticed that the hit rate is not homogeneous on all the ROCs in the module. ROCs zero to seven have higher hit rates than ROCs eight to 15. The module has two so-called channels, each of which are responsible of the readout of the eight ROCs on one side of the module. Both channels are then merged in the TBM. One of the channels seems to have problems reading out the totality of the data if the hit rate is too high. This might be due to problems with either the TBM or with the beta version of the testboard which was used for the

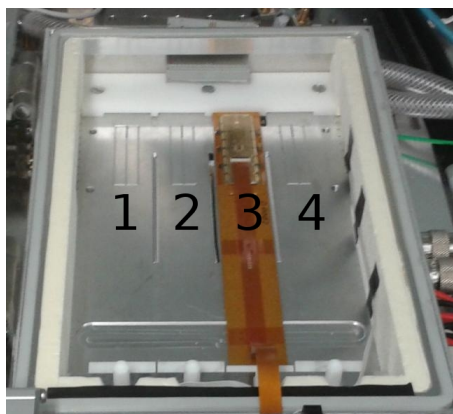


Figure 37: *The test setup has four positions on which modules can be installed to be tested. There are numbered from one to four.*

readout of the module. This is currently being investigated.

It can also be noticed that ROCs zero to two and 13 to 15 have lower hit rates than the others. This is not a problem of the readout of the module but is due to the profile of the primary beam. Its intensity is decreasing from ROCs seven and eight to ROCs zero and 15. The sharpness of the cut off between ROCs two and three and ROCs 12 and 13 can be explained by the fact that although many rows of the ROCs have been deactivated to exclude shadows, on ROCs two and 13, a little shadow from the signal and power cable remains. This was not removed in order to have a large enough active part of the ROCs in order to get statistically significant results.

Furthermore, it can be observed on Figure 39 that the average hit rate on the entire module is varying between the different test positions in the test setup. The first row in Table 7 gives the hit rate for every position averaged over all ROCs. It can be seen that it is almost identical for positions two and three but that it is lower on positions one and four. In order to get these results, all four test positions were shifted to the left by 1.7 cm because before the shift, the X-ray beam centre was too far to the left as can be seen in Figure 38.

In order to get the same hit rate over all four positions, the tube settings can be modified during measurements on positions one and four. The aim is to take measurements on modules in positions two and three, and then to modify the voltage or the tube current before taking measurements on positions one and four to increase the hit rate on those two positions. To calculate how the tube setting must be modified, it will be assumed that the hit rate increases linearly with the incoming quantity of radiation of the X-ray beam, which is the number of photons in the beam, at a constant irradiation time and distance from the source. The average hit rate for positions one and four is 87.58 MHz/cm<sup>2</sup> and 111.45 MHz/cm<sup>2</sup> for positions two and three. Therefore, to get the same hit rate on all four positions, it needs to be increased by 27% on positions one and four. The quantity  $q$  of X-radiation of the primary beam is given by [20]:

$$q \propto \frac{U^2 \cdot i \cdot t \cdot Z}{d^2} \quad (5)$$

where

- $i$  is the current in the X-ray tube
- $U$  is the voltage applied between the anode and cathode
- $t$  is the irradiation time
- $Z$  is the atomic number of the anode material and

- $d$  is the distance between the source and the measurement point.

In the following calculation, the primed quantities are those which represent the new tube settings. Keeping the irradiation time, the applied current and the distance to the source constant, the ratio between the voltage applied for measurements on positions one and four and the voltage for positions two and three becomes:

$$\begin{aligned}\frac{U'}{U} &= \sqrt{\frac{q'}{q}} \\ &= \sqrt{1.27} \\ &\simeq 1.13\end{aligned}\tag{6}$$

$$\Rightarrow U' = 1.13 \cdot U\tag{7}$$

$$\Rightarrow U' = 33.9 \text{ kV} \quad \text{for } U=30 \text{ kV}\tag{8}$$

Noting that only integer values for current and voltage can be chosen, the voltage applied between cathode and anode must be raised from 30 keV to 34 keV for measurements on positions one and four in order to get a hit rate of around 111.45 MHz/cm<sup>2</sup> on all four test positions. It is also possible to increase the current instead of the voltage. In this case, the current would have to be set to 6 mA instead of 5 mA.

In section 3.3.1, it was shown that the intensity of the secondary emission coming from the targets is isotropic at constant distance from the source of the fluorescence. It will now be studied if this also reflects on the hit rate on a module. Figures 40 and 41 show the hit rate from the secondary emission of Mo and Sn target materials for all ROCs on the four test positions. The tube settings for these results were 60 kV and 30 mA and the measurement acquisition time was 100 s. Hit rates on ROCs two and 13 are lower than for the others for the same reason as above. It can be read in Table 7 which shows the average hit rates on the module for all four positions that the average hit rate from the Mo target is around 0.5 MHz/cm<sup>2</sup> and 0.17 MHz/cm<sup>2</sup> for Sn. The only significant difference is that the hit rate slightly decreases from position one to four. It decreases by 9.2% from position one to position four for Mo and by 8.4% for Sn. This is expected because the distance between the target materials and the sensor increases from position one to four.

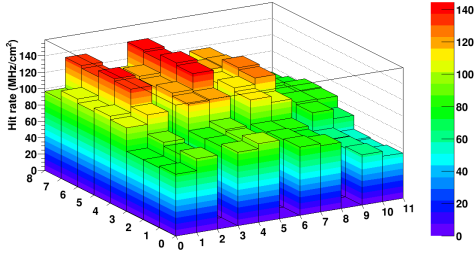


Figure 38: *Hit rates of the primary beam on the four test positions (Old emplacement). The hit rates are not homogeneous, they are higher on positions one, two and three than on position four. The hit rates on each ROC in the module are also inhomogeneous. Columns 1,2 : Position 1  
Columns 4,5 : Position 2  
Columns 7,8 : Position 3  
Columns 10,11 : Position 4*

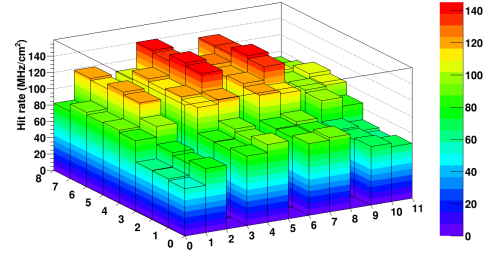


Figure 39: *Hit rates of the primary beam on the four test positions (New emplacement). The hit rates are largest on positions two and three, and are decreasing on positions one and four. The remaining inhomogeneities can be explained by the beam profile.*

Table 7: *Average hit rates on the module on the four test positions. For Sn and Mo, the hit rates are slightly decreasing from position one to four. For the primary beam, the highest hit rates used to be on positions one and two. With the new emplacement, they are on positions two and three.*

Hit rates (MHz/cm <sup>2</sup> )	P.1	P.2	P.3	P.4
Primary Beam (New emplacement)	88.64	111.8	111.1	86.51
Primary Beam (Old emplacement)	103.3	113.6	101.9	71.63
Mo	0.5263	0.5115	0.4953	0.4781
Sn	0.1825	0.1769	0.1746	0.1672

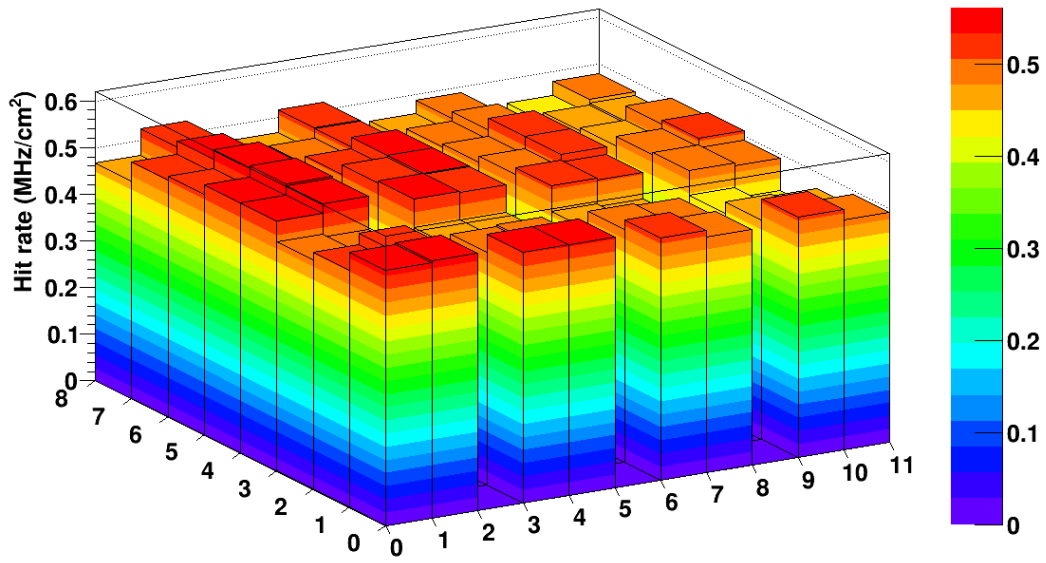


Figure 40: *Homogeneity of the Mo fluorescence on the four test positions. The hit rates of all ROCs on the four positions are similar except for a small decrease from position one to four.*

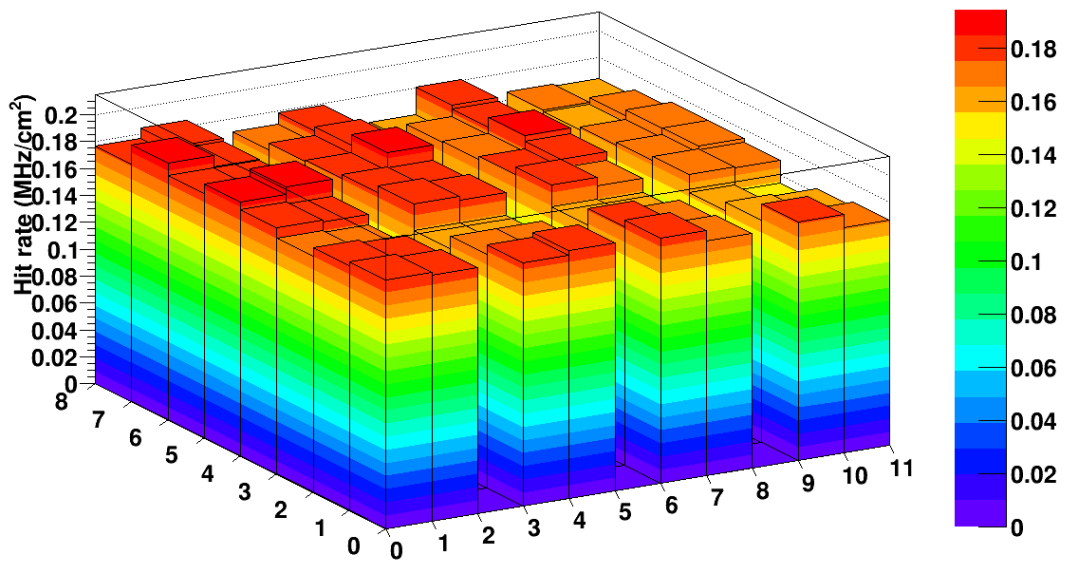


Figure 41: *Hit rates of the Sn fluorescence on the four test positions. The rates are slightly decreasing from positions one to position four, but are similar for all ROCs in the module.*

## 6 Conclusions and outlooks

### 6.1 Key results

The aim of this work was to study if by using filters, the setup used for Vcal calibrations of modules for the CMS pixel detector can be improved. In the first part, the X-radiation in the setup was studied with a spectrometer. It was verified that the intensity of the X-radiation decreases with increasing distance between sensor and target materials. The energy of the  $K_\alpha$  line is the same on all positions for every target material as expected and is in very good agreement with theoretical values. The effect of filters on the secondary emission created by different target elements was studied using filters for Mo, Ag and Sn target materials. It could be seen that with filters, only 6.1 %, respectively 5.2 % and 4.8 % of the  $K_\beta$  line in the Mo, Ag, and Sn spectra remains which shows that filters remove most of the  $K_\beta$  line. Part of the background is removed by the filters as well. However, the  $K_\alpha$  emission line is also attenuated. For Mo, the intensity is reduced by 40 % , for Ag, it is 47 % and for Sn 51 %. This implies that to obtain the same number of detected X-rays, the measurement acquisition time would have to be increased by a factor two. A small contribution from the  $K_\alpha$  emission line of the filter material can be observed in the spectra but its intensity is negligible.

It was then tested if the effect filters have on the measured spectra is reflected on the Vcal calibration of ROCs. First, the spectra measured with a single chip module with and without the use of filters have been studied. Since the energy resolution of the ROC is not as good as the one from the spectrometer, the  $K_\alpha$  and  $K_\beta$  emission lines are combined in a broader peak whose mean is shifted to higher Vcal values than the  $K_\alpha$  peak. When filters which remove the  $K_\beta$  line are used, it is expected that the energy peak is narrower and at lower Vcal units. It was found that the secondary emission emitted by the Mo target is modified as expected when a filter is added. The sigma of the Gaussian fit on the energy peak is 1.83 Vcal units smaller with filter than without. The mean of the fit also decreases by 1.14 Vcal units. While the width of the spectrum of the Ag fluorescence also decreases when a filter is added, the mean of the peak is almost unaffected by the filter. For Sn, the mean of the peak even increases by 3.87 Vcal units. No explanation for this results was found. Using the values found for the mean of the energy peak, a Vcal calibration with and without filters was carried out for a digital ROC. The slope is slightly less steep with filters than without. As a consequence, the offset increases with filters. It has to be remembered however that there is a certain uncertainty on these results since the values for the slope and the offset were obtained with a linear fit that does not describe the data very well for the Vcal calibration with filters. A Vcal calibration of a digital module was carried out as well. For this module, neither the average of the slope nor the offset of the 16 ROCs was significantly modified by

the addition of filters.

Finally, the hit rate on every ROC in the module on all four test positions was measured. With irradiation from the primary beam, it was found that the hit rate was much lower on position four than for the others. The test setup for modules was therefore shifted to the left by 1.7 cm. A new measurement confirmed that the hit rate is more homogeneous on the four positions after the shift while still being slightly lower on positions one and four compared to positions two and three due to the gradient in the beam profile. It was calculated that the voltage between cathode and anode of the X-ray tube needs to be increased by 13% or that the current needs to be increased by 27% when taking measurements on positions one and four to obtain similar hit rates. The irradiation with fluorescence from Mo and Sn targets showed that the hit rate is in this case mostly homogeneous except for a light decrease from positions one to four as the distance to the target materials increases.

## 6.2 Further work and outlooks

According to the results of the Vcal calibration with and without filter obtained for the digital module which has more statistics than the single chip module since it takes the average over 16 ROCs instead of one, filters do not have a significant impact on the Vcal calibration of ROCs. Consequently filters do not seem to be an improvement to the module calibration setup. This work however only tested one ROC and one digital modules such that it is important to study the influence of filters on more ROCs and modules to see if the results found here are representative.

If after further measurements it is decided to include filters in the permanent setup, longer measurement acquisition times would have to be accepted due to the attenuation of the  $K_\alpha$  line by filters. If filters are used in the permanent setup, they should carefully be removed from their packaging. The Ni filter for the Cu target could then also be used to carry out the Vcal calibration with four instead of three points which would increase the precision with which the slope and offset can be determined. Before installing filters however, it is necessary to investigate why for the Ag and particularly for the Sn targets, the effect of filters on the mean and the width of the energy peak is not what is expected and observed in the spectra for Mo measured with the single chip module.

## Acknowledgements

I would like to express my gratitude to Prof. Dr. Rainer Wallny and Dr. Andrey Starodumov for their valuable supervision and guidance. I would also like to thank Jan Hoß and all other members of the ETH Pixel Detector Group for their help and advice throughout the course of this work.



# Appendix

## Fits on the energy spectra measured with a single chip module with and without filter

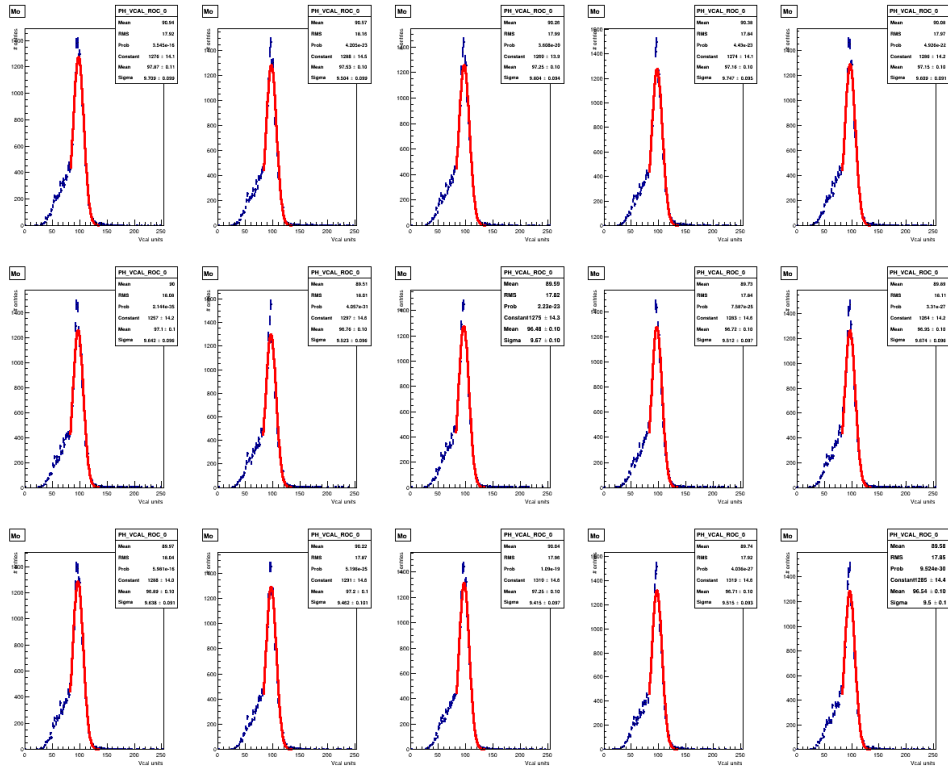


Figure 42: Fits for 15 measurements for Mo spectra without filter

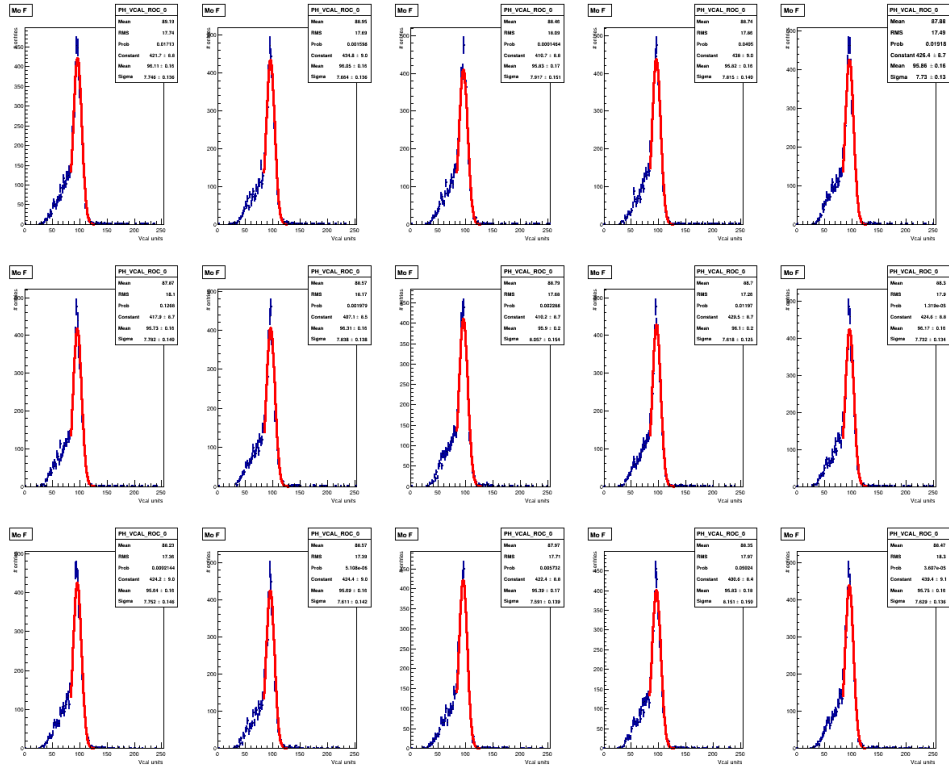


Figure 43: Fits for 15 measurements for Mo spectra with filter

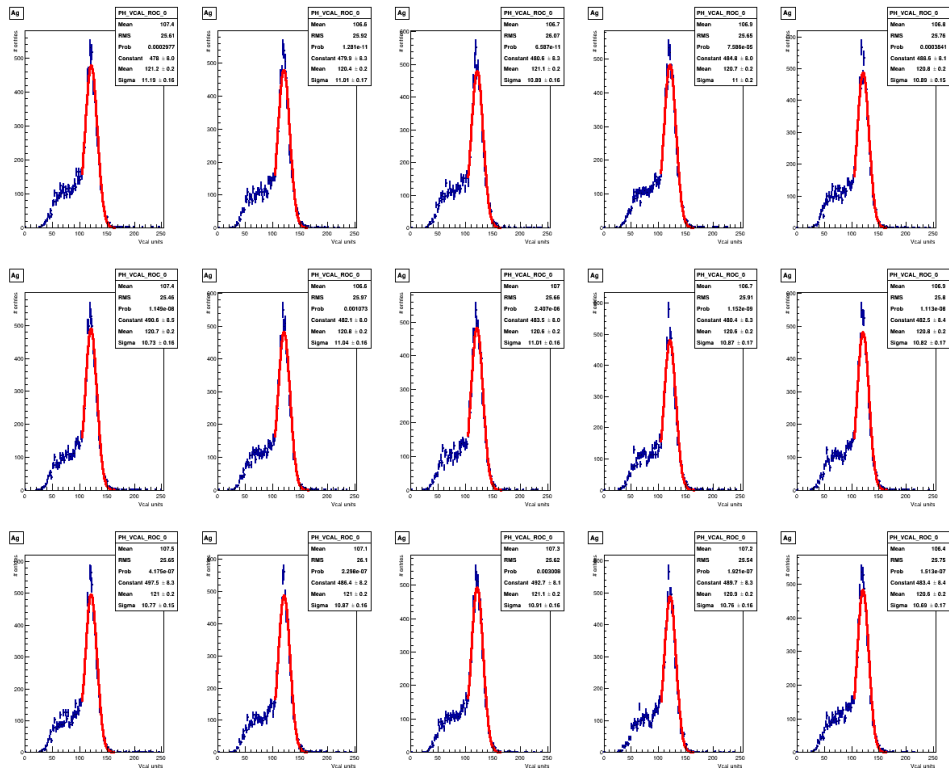


Figure 44: Fits for 15 measurements for Ag spectra without filter

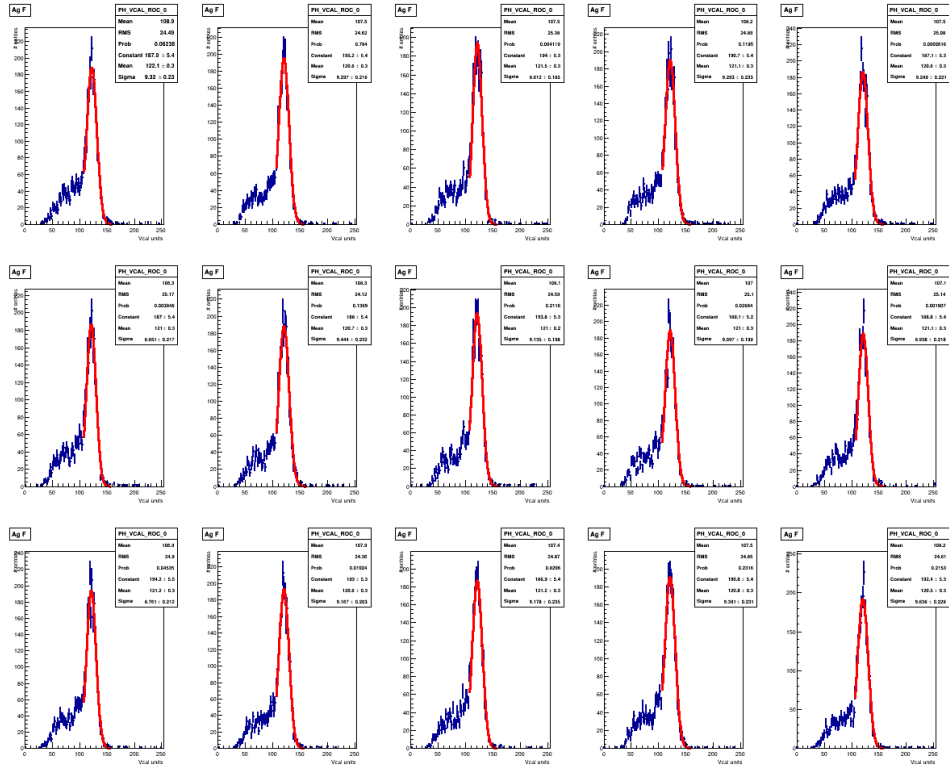


Figure 45: *Fits for 15 measurements for Ag spectra with filter*

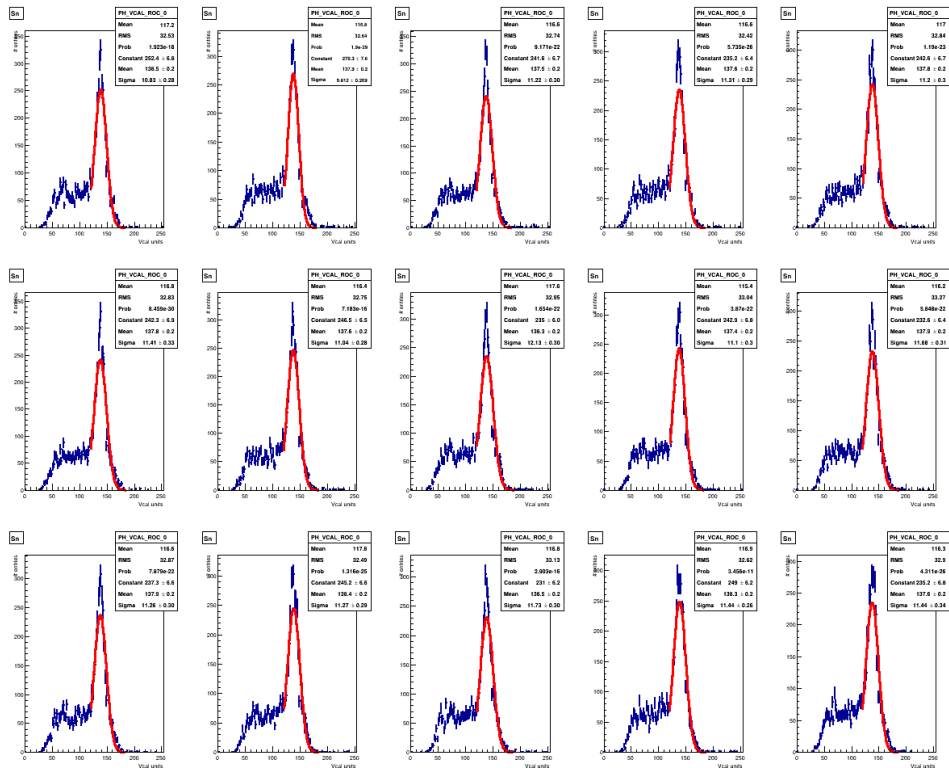


Figure 46: *Fits for 15 measurements for Sn spectra without filter*

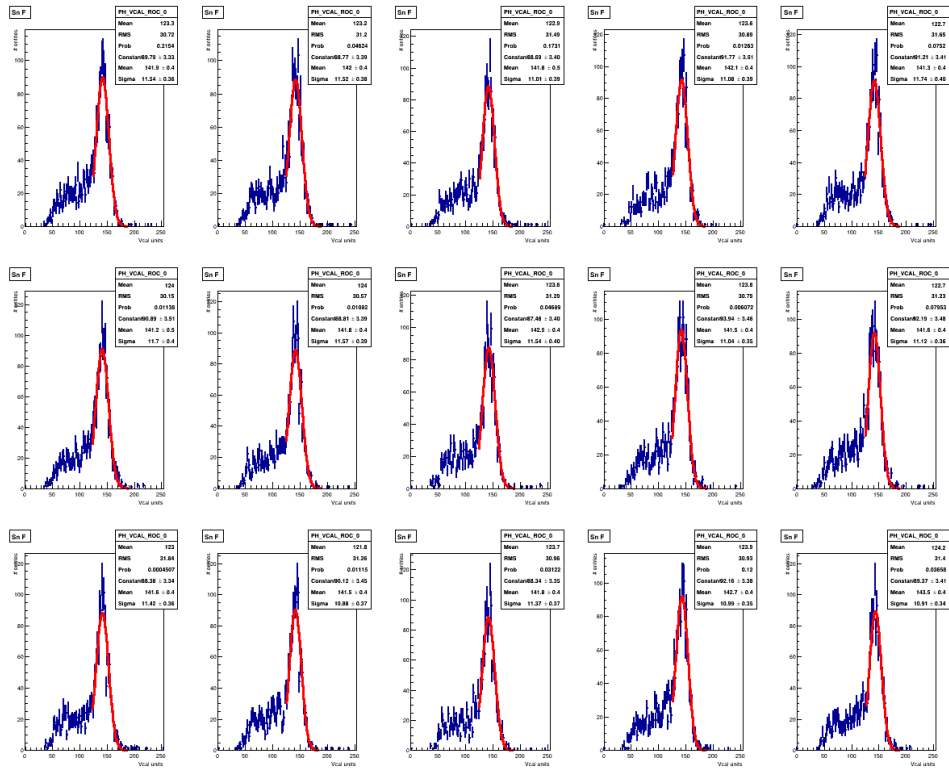


Figure 47: *Fits for 15 measurements for  $Sn$  spectra with filter*

# Fits on the spectra for Mo, Ag and Sn measured with a digital module with and without filter

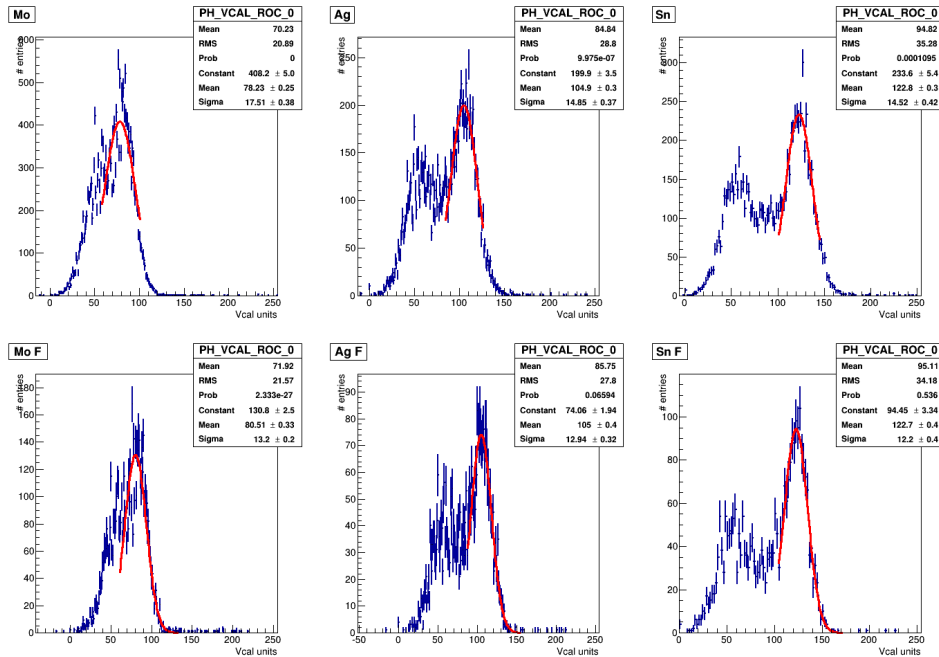


Figure 48: *ROC 0 - Top row: Without filter - Bottom Row: With filter*

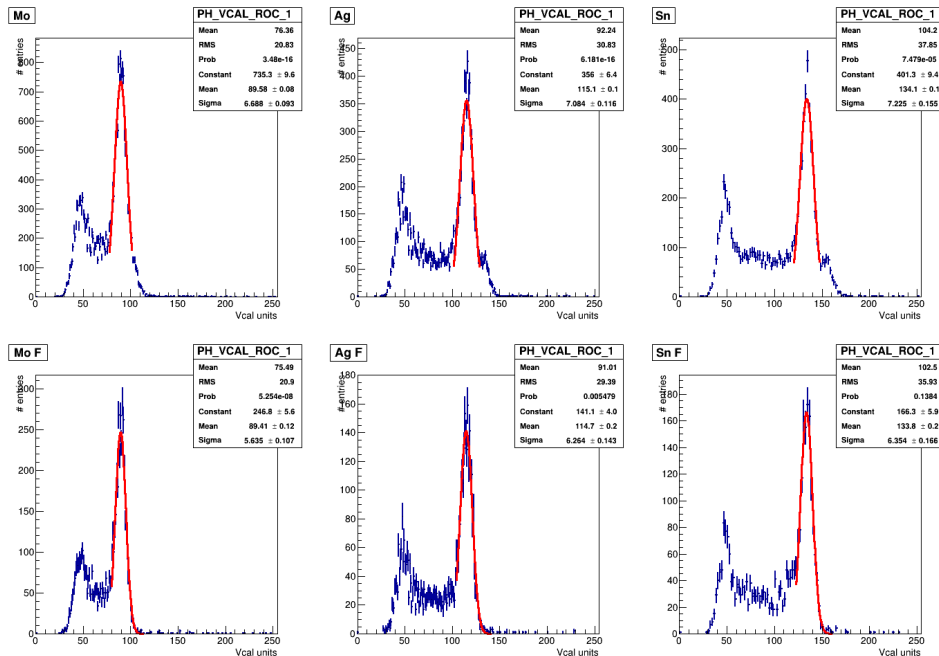


Figure 49: *ROC 1*

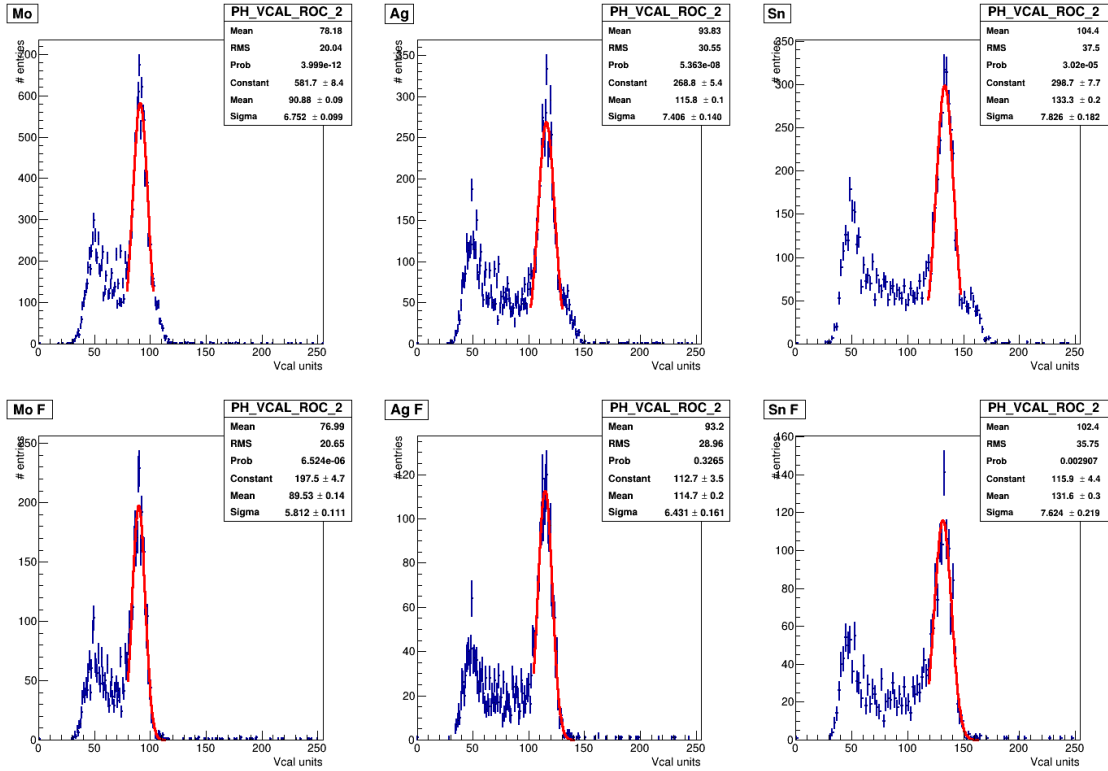


Figure 50: *ROC 2*

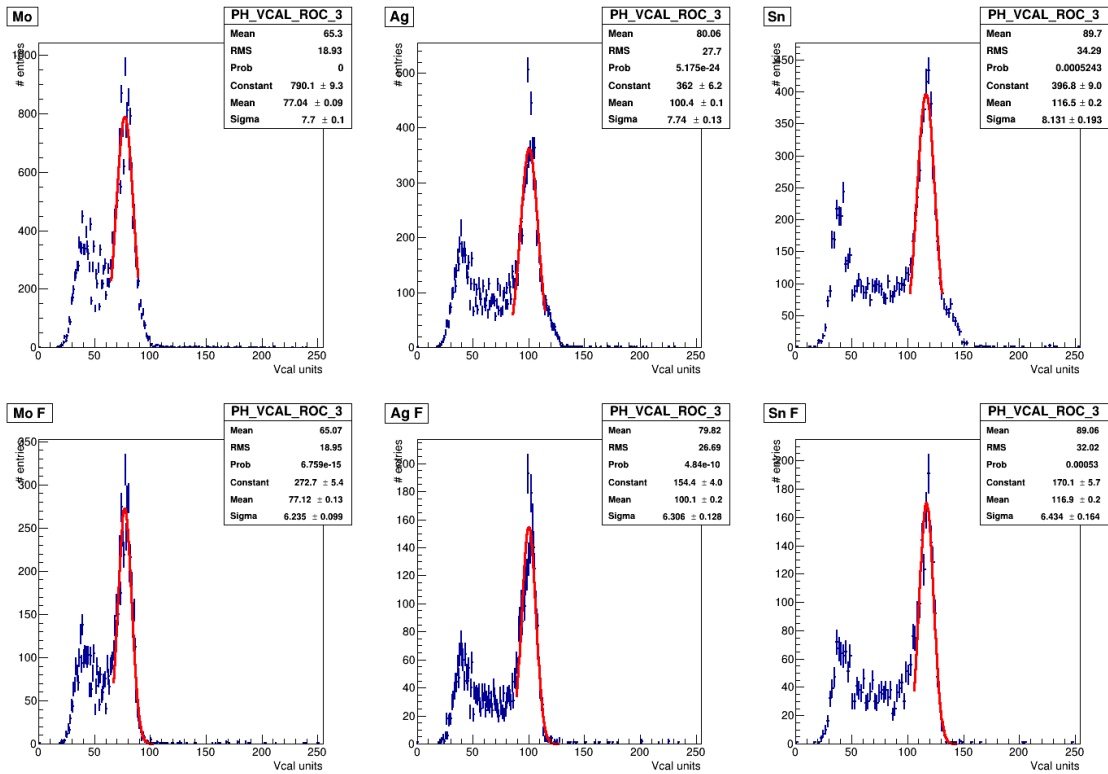


Figure 51: *ROC 3*

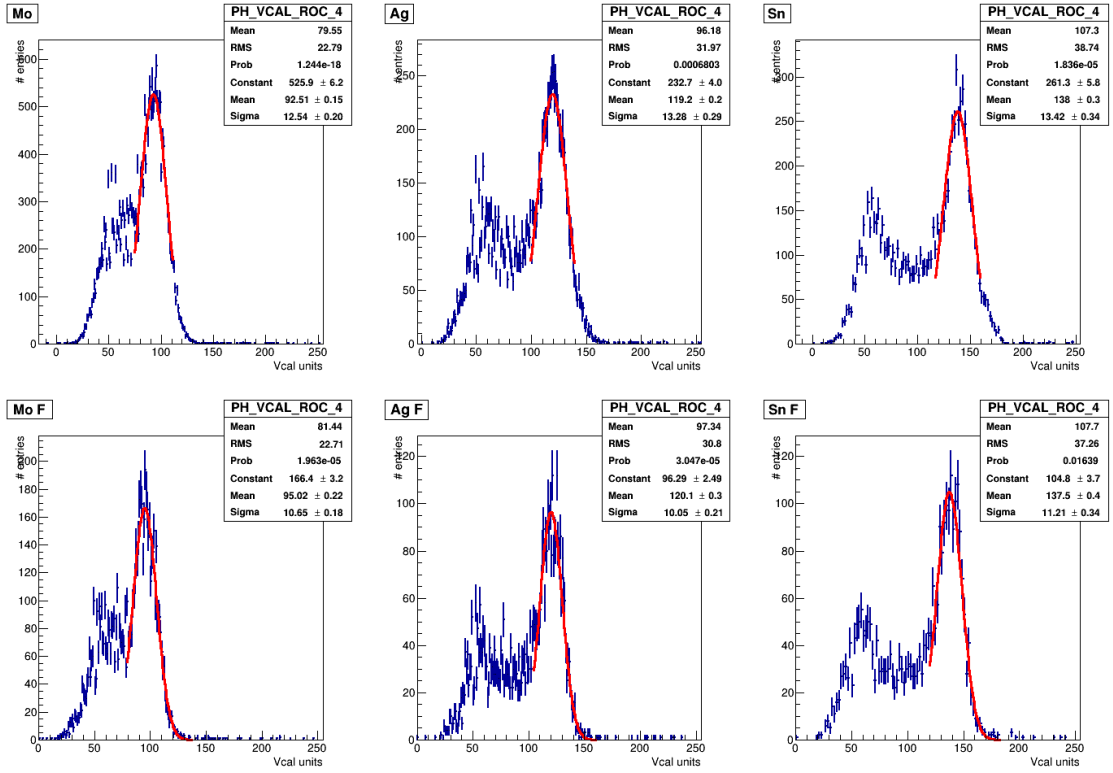


Figure 52: *ROC 4*

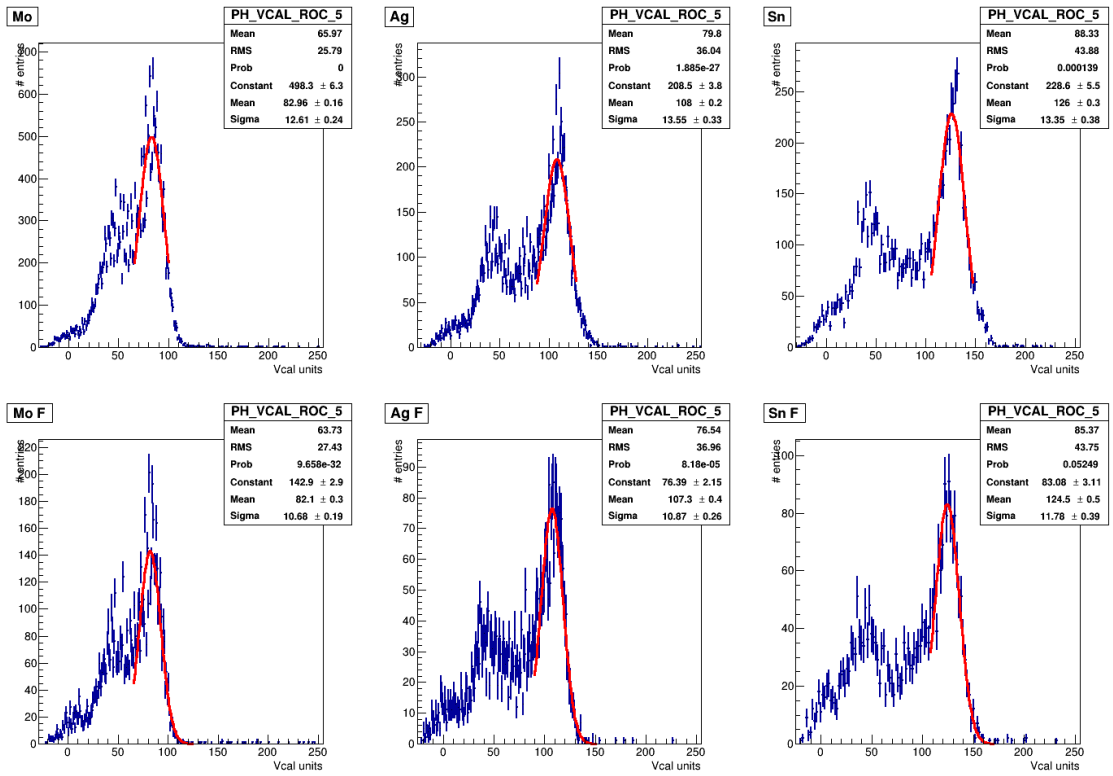


Figure 53: *ROC 5*

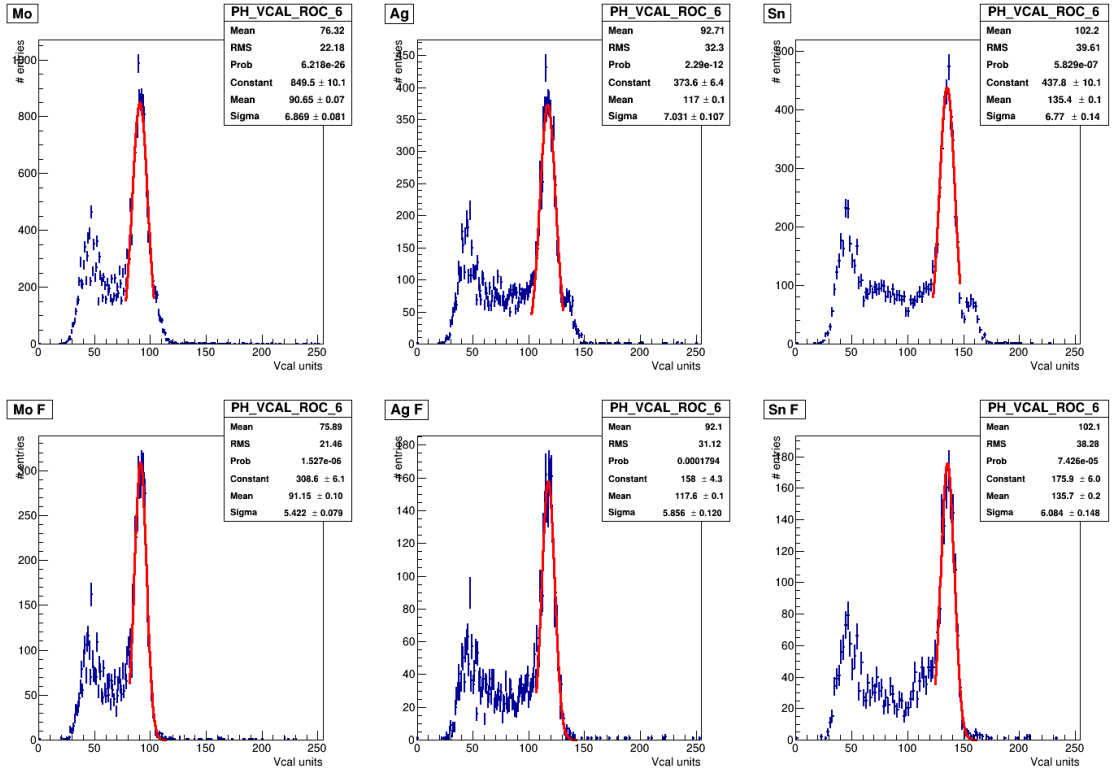


Figure 54: *ROC 6*

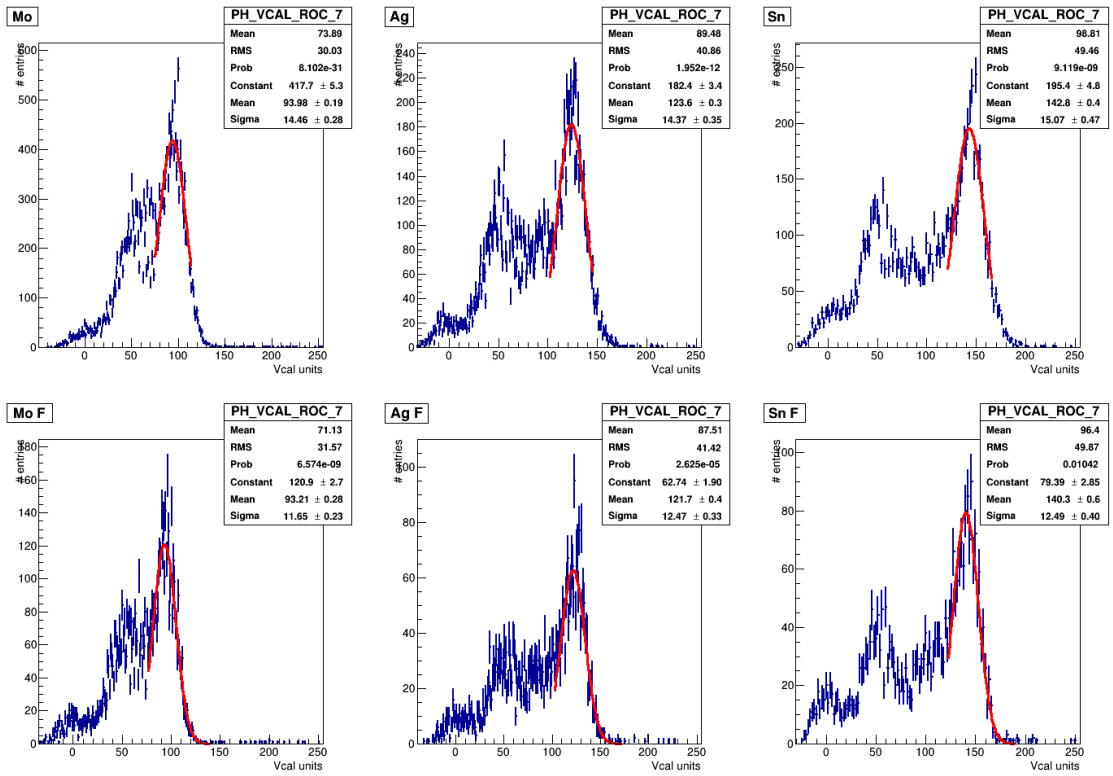


Figure 55: *ROC 7*



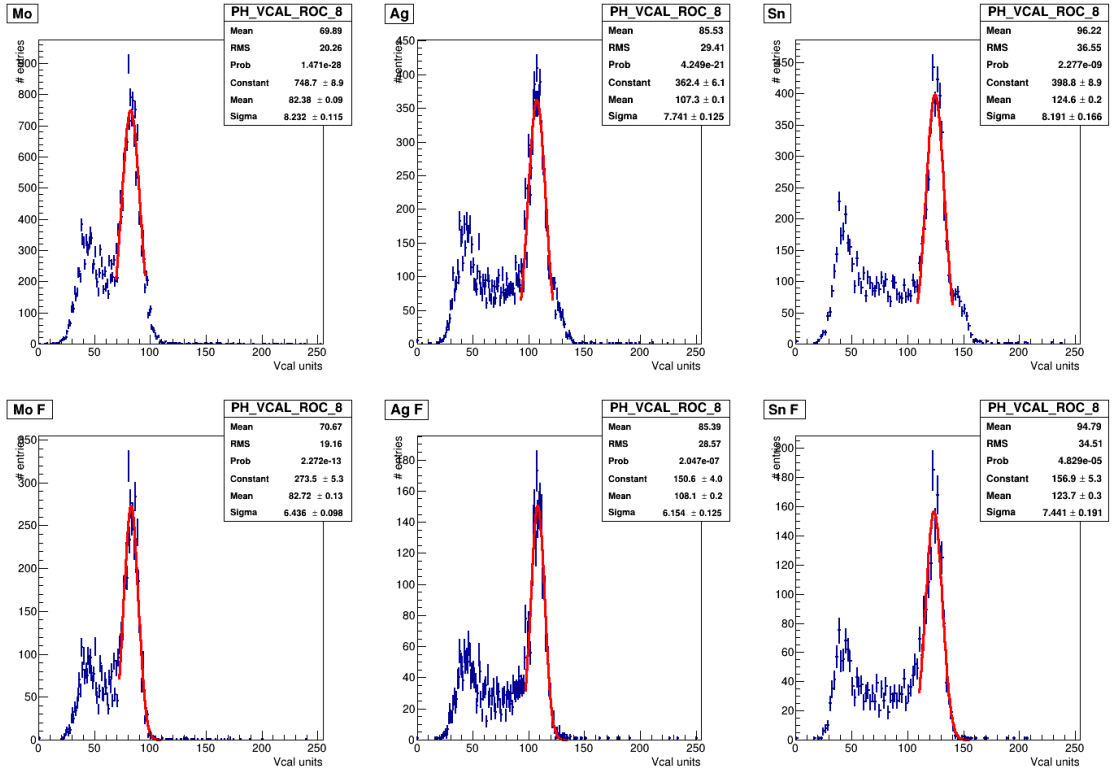


Figure 56: *ROC 8*

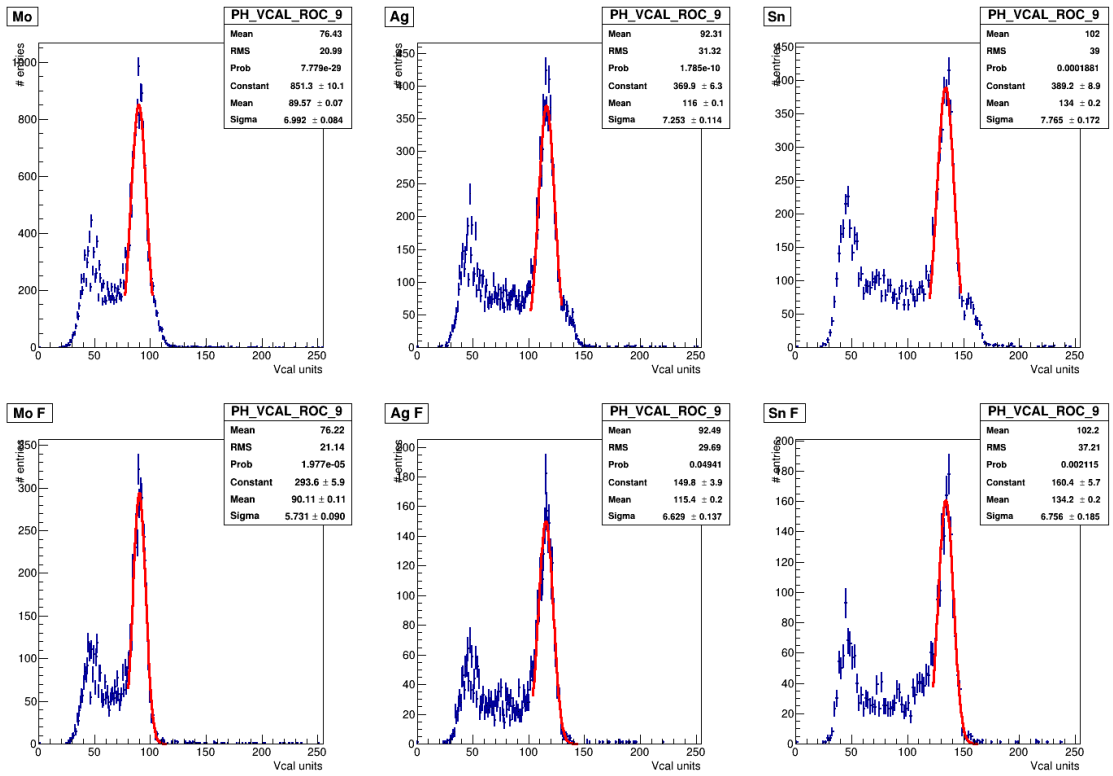


Figure 57: *ROC 9*

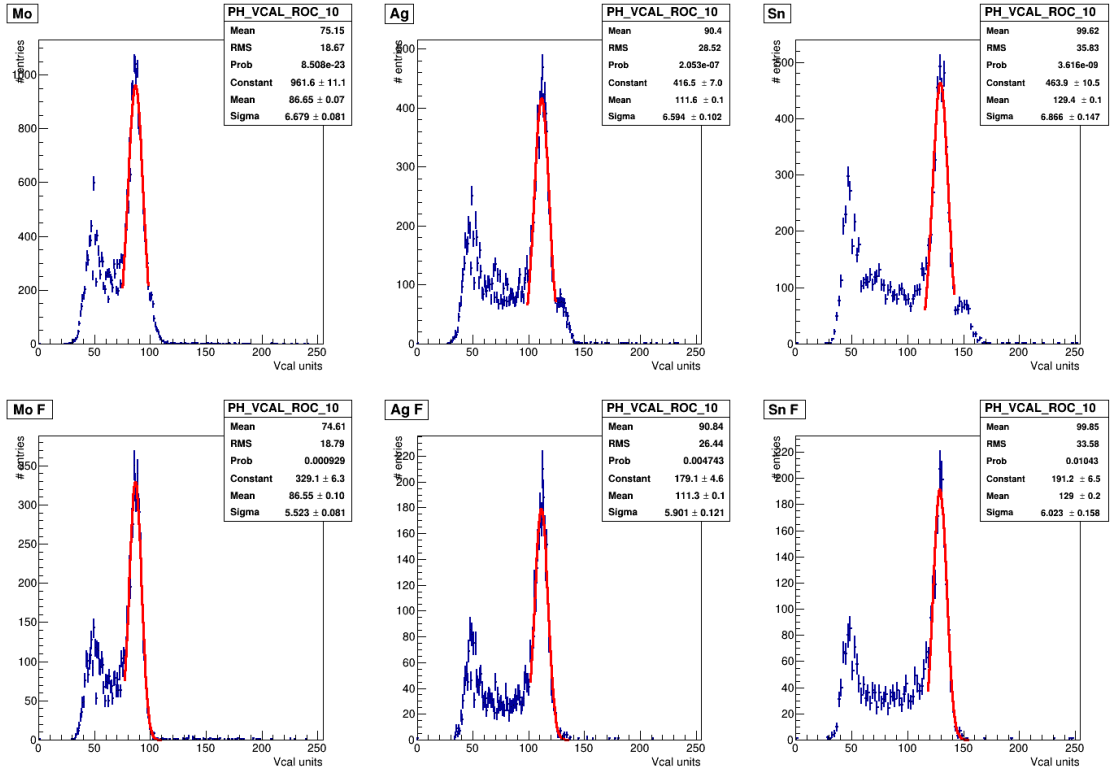


Figure 58: *ROC 10*

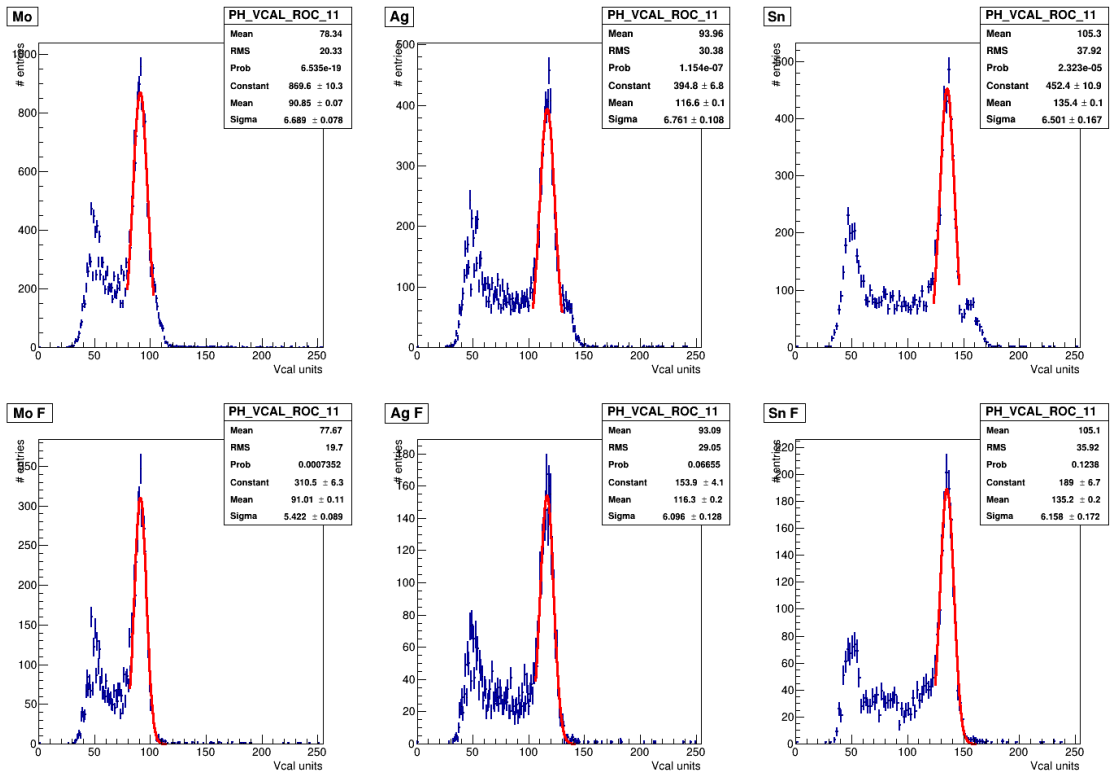


Figure 59: *ROC 11*

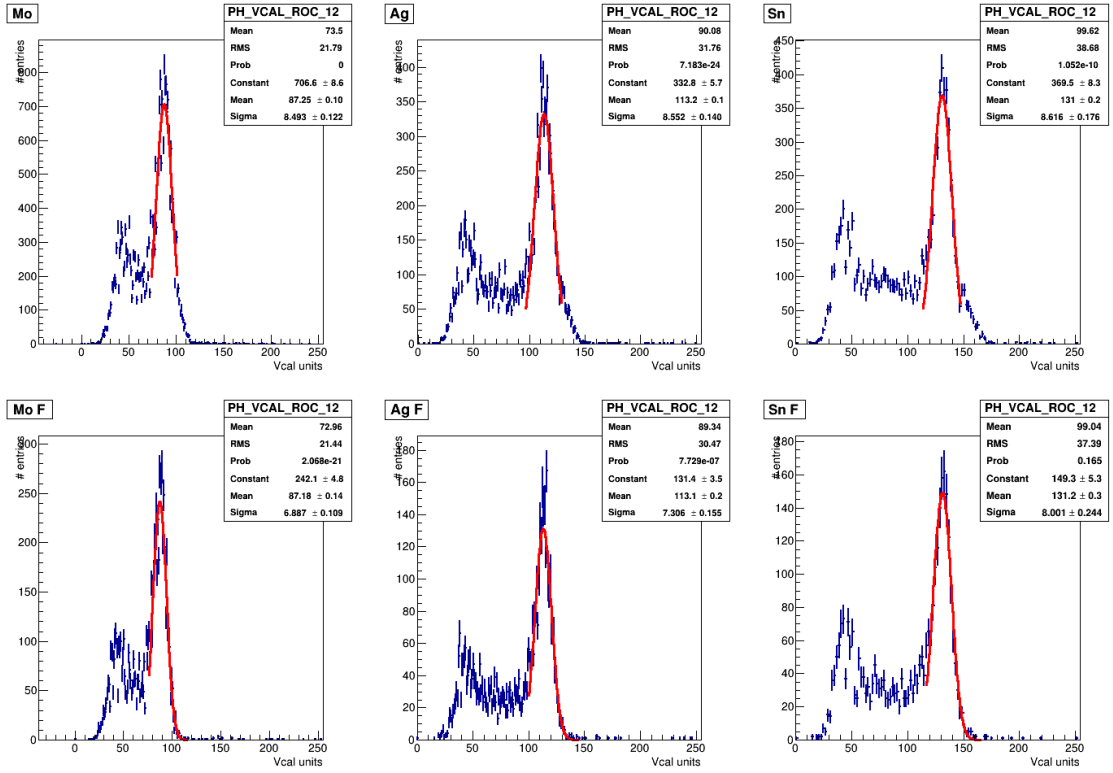


Figure 60: *ROC 12*

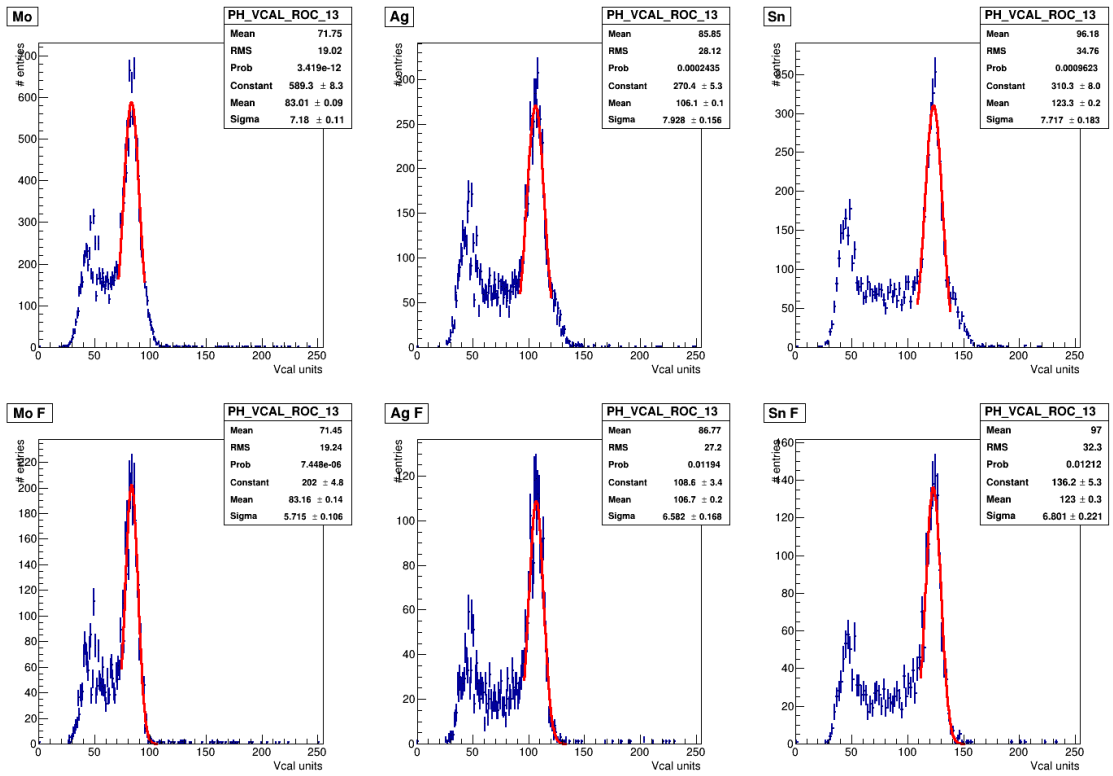


Figure 61: *ROC 13*

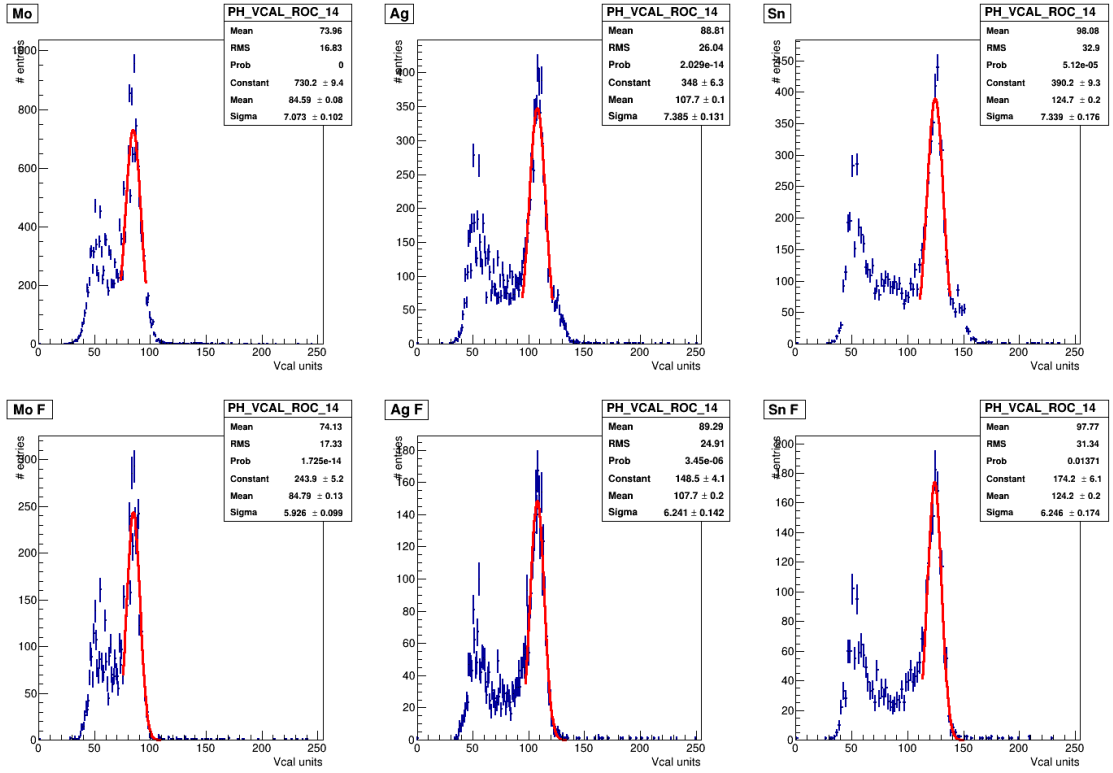


Figure 62: *ROC 14*

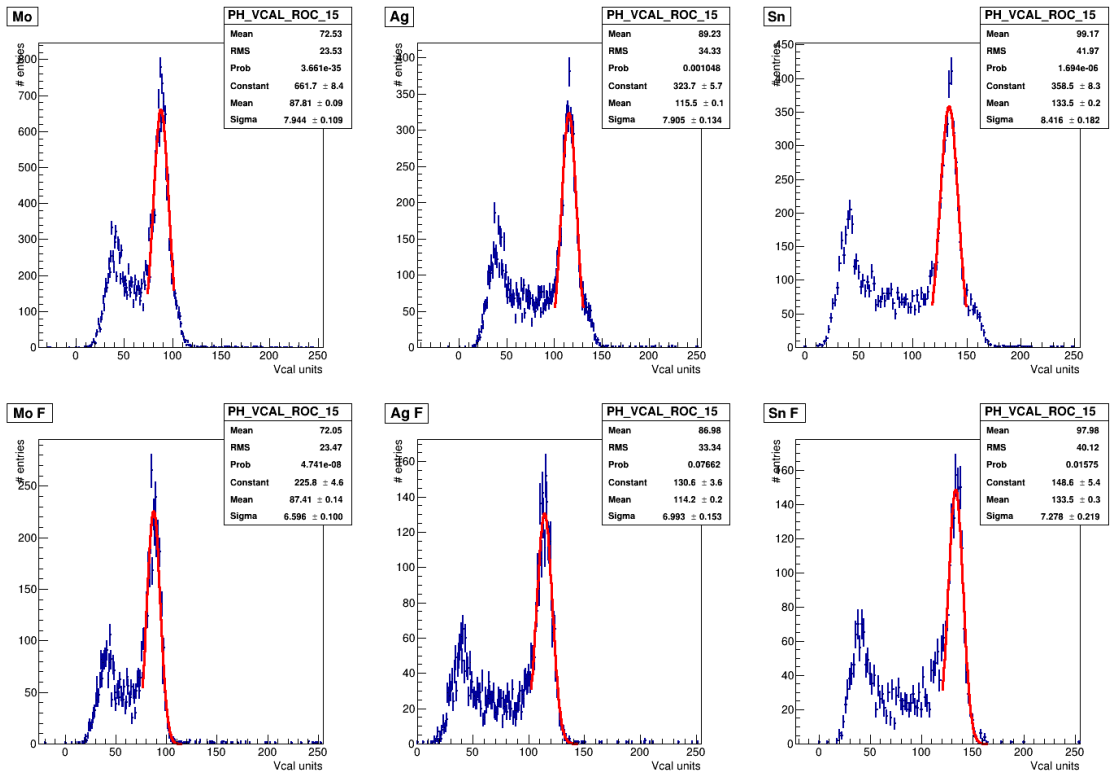


Figure 63: *ROC 15*

# Vcal calibration of a digital module

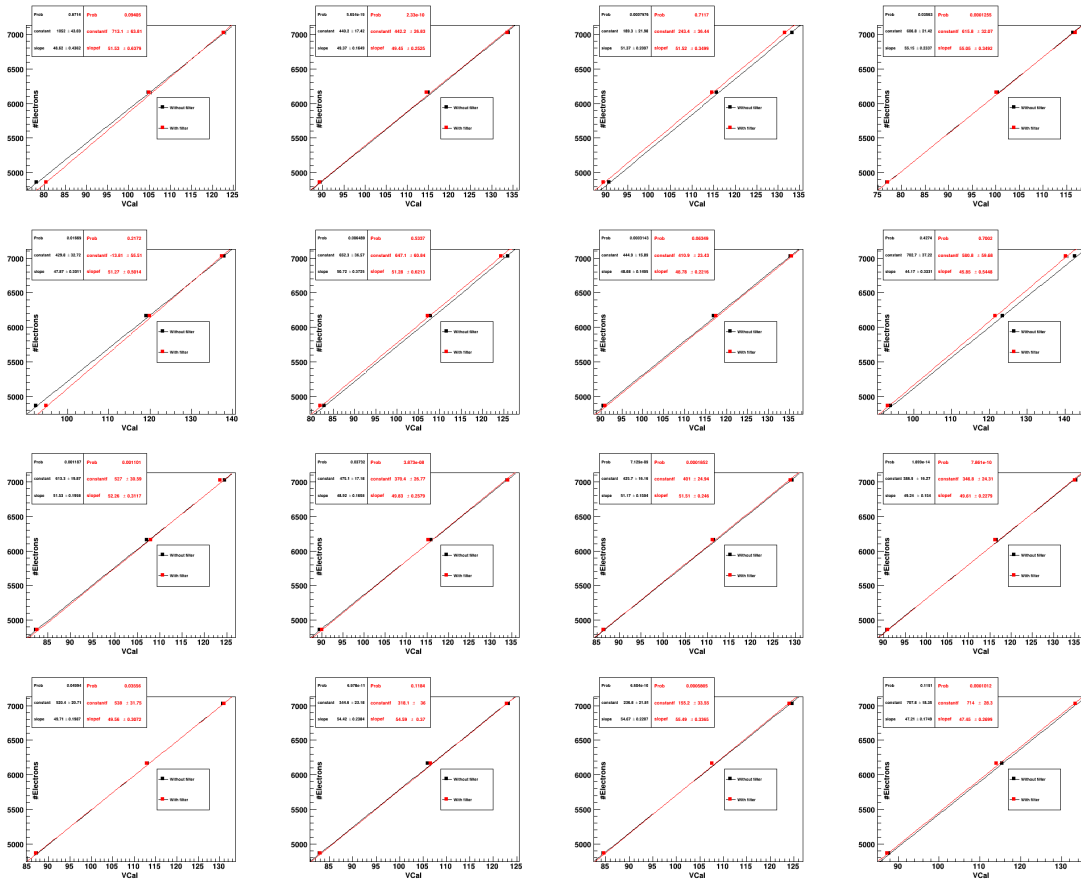


Figure 64: *Vcal* calibration of a digital module

# Values of the $\sigma$ of the Gaussian fit on the spectra with and without filter for fifteen measurements

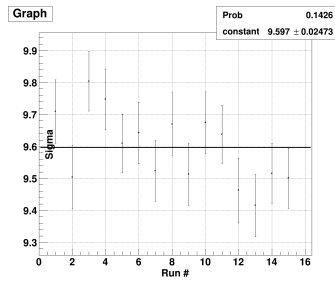


Figure 65: *Mo* -  
*Without filter*

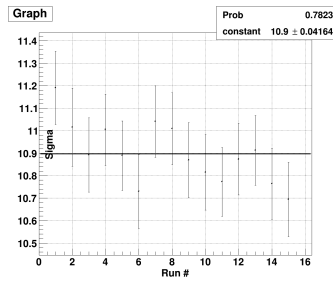


Figure 66: *Ag* -  
*Without filter*

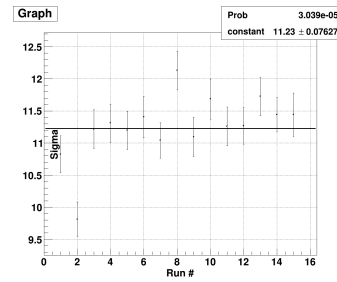


Figure 67: *Sn* -  
*Without filter*

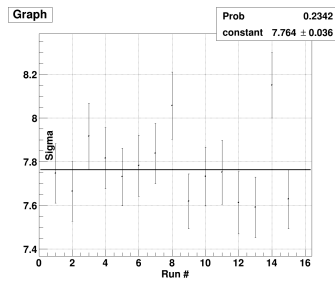


Figure 68: *Mo* -  
*With filter*

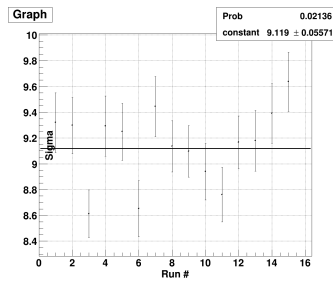


Figure 69: *Ag* -  
*With filter*

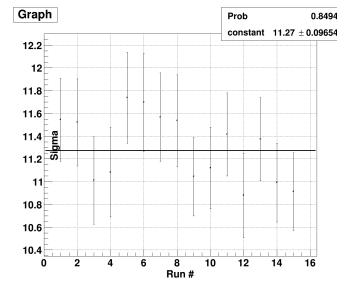


Figure 70: *Sn* -  
*With filter*

# Values of the mean of the Gaussian fit on the spectra with and without filter for fifteen measurements

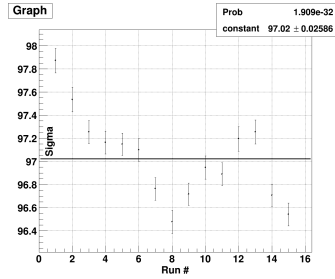


Figure 71: *Mo* -  
*Without filter*

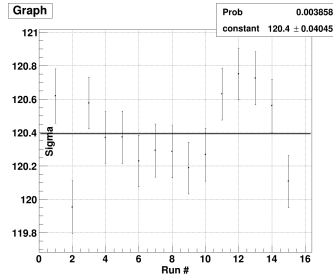


Figure 72: *Ag* -  
*Without filter*

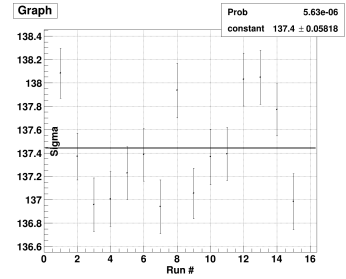


Figure 73: *Sn* -  
*Without filter*

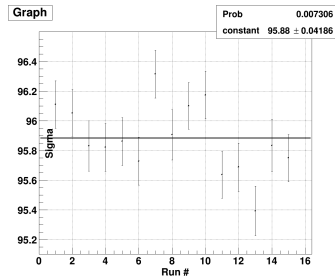


Figure 74: *Mo* -  
*With filter*

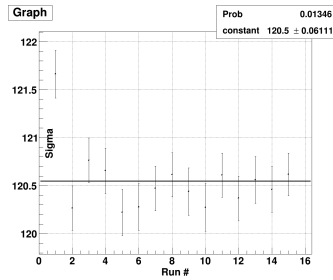


Figure 75: *Ag* -  
*With filter*

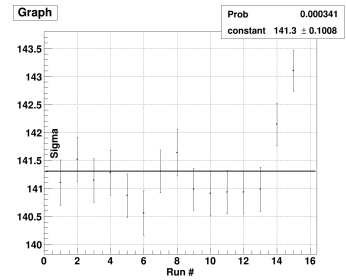


Figure 76: *Sn* -  
*With filter*

## References

- [1] CMS Collaboration, *Observation of a new boson at a mass of 125 GeV with the CMS experiment at the LHC*, [Online], 2012,  
<http://arxiv.org/abs/1207.7235>
- [2] ATLAS Collaboration, *Observation of a new particle in the search for the Standard Model Higgs boson with the ATLAS detector at the LHC*, [Online], 2012,  
<http://arxiv.org/abs/1207.7214>
- [3] L. Taylor, *CMS detector design*, [Online], 23 November 2011,  
[https://cms-docdb.cern.ch/cgi-bin/PublicDocDB/RetrieveFile?docid=11514&version=1&filename=cms\\_120918\\_03.png](https://cms-docdb.cern.ch/cgi-bin/PublicDocDB/RetrieveFile?docid=11514&version=1&filename=cms_120918_03.png)
- [4] D. Acosta *et al.*, *CMS Physics: Technical Design Report - Volume I : Detector Performance and Software*, [Online], 2006,  
<http://cds.cern.ch/record/922757/files/lhcc-2006-001.pdf>
- [5] Cian O’Luanaigh, *CERN announces LHC restart schedule*, [Online], 2014,  
<http://home.web.cern.ch/about/updates/2014/06/cern-announces-lhc-restart-schedule>
- [6] V. Karimäki *et al.*, *The CMS tracker system project: Technical Design Report*, [Online], 1997,  
[http://cds.cern.ch/record/368412/files/Tracker\\_TDR.pdf](http://cds.cern.ch/record/368412/files/Tracker_TDR.pdf)
- [7] A. Dominguez *et al.*, *CMS Technical Design Report for the Pixel Detector Upgrade*, [Online], 16 August 2012,  
<http://cds.cern.ch/record/1481838/files/CMS-TDR-011.pdf>
- [8] D. C. Contardo, *CMS prepares for Pixel and HCAL upgrades*, [Online], 30 October 2012,  
<http://cms.web.cern.ch/news/cms-prepares-pixel-and-hcal-upgrades>
- [9] D. Villar, *Qualification of the X-ray test setup for the Vcal calibration of the CMS pixel detector readout chip*, [Online], 6 July 2012,  
<http://cmspixel.phys.ethz.ch/publ/2012-daniel.pdf>
- [10] National Institute of Standards and Technology (NIST), *X-ray Transition Energies Database* [Online],  
<http://physics.nist.gov/PhysRefData/XrayTrans/Html/search.html>
- [11] Amptek, *Complete X-Ray Spectrometer X-123* [Online],  
<http://www.amptek.com/pdf/x123.pdf>



- [12] D. Pitzl, *Digital ROC beam test results* [Online], 24 August 2012  
[http://cms.desy.de/sites/site\\_cms/content/e53612/e90917/e155178/e157748/e169877/240812-dp.pdf](http://cms.desy.de/sites/site_cms/content/e53612/e90917/e155178/e157748/e169877/240812-dp.pdf)
- [13] B. Meier, *CMS pixel detector with new digital readout architecture* [Online], 5 January 2011  
[http://iopscience.iop.org/1748-0221/6/01/C01011/pdf/jinst11\\_01\\_c01011.pdf](http://iopscience.iop.org/1748-0221/6/01/C01011/pdf/jinst11_01_c01011.pdf)
- [14] J. Hoß, *X-Ray Calibration of Pixel Detector Modules for the Phase I Upgrade of the CMS Experiment* [Online], 27 September 2012  
<http://ekp-invenio.physik.uni-karlsruhe.de/record/48180/files/iekp-ka2012-17.pdf>
- [15] L. Hoppenau, *Characterization of the Analog and Digital CMS Pixel Readout Chip after Irradiation* [Online], 25 July 2013  
[http://cmspixel.phys.ethz.ch/publ/Thesis\\_Hoppenau.pdf](http://cmspixel.phys.ethz.ch/publ/Thesis_Hoppenau.pdf)
- [16] R. Guinebretière, *X-Ray Diffraction by Polycrystalline Materials* (Wiley-ISTE, March 2007)
- [17] M. L. Jackson, *Soil Chemical Analysis: Advanced Course* (UW-Madison Libraries Parallel Press, January 2005)
- [18] Marco Rossini, *Personal conversation* (April 2014)
- [19] H. Spieler, *"Silicon Detectors" Basic Concepts I* [Online], 23 October 1998  
[http://www-group.slac.stanford.edu/sluc/lectures/detector\\_lecture\\_files/detectorlectures\\_6.pdf](http://www-group.slac.stanford.edu/sluc/lectures/detector_lecture_files/detectorlectures_6.pdf)
- [20] K. Thayalan, *Basic Radiological Physics* (Jaypee Brothers Publishers, 2008)
- [21] J. Hook, H. Hall, *Solid State Physics* (John Wiley & Sons, 2013)